Single-cell analysis characterizes non-enhancing region of recurrent high-grade glioma

Kunal S. Patel[1]*, Kaleab K. Tessema[2]*, Riki Kawaguchi[3], Alvaro G. Alvarado[2], Sree Deepthi Muthukrishnan[2], Akifumi Hagiwara[4], Vivek Swarup[5], Linda M. Liau[1], Anthony Wang[1], William Yong[6], Daniel H. Geschwind[3], Ichiro Nakano[7], Steven A. Goldman[8,9], Richard Everson[1#], Benjamin M. Ellingson[1,4#], Harley I. Kornblum[2,10#]

[1]Department of Neurosurgery, David Geffen School of Medicine at UCLA, Los Angeles, CA

[2]The Intellectual and Developmental Disabilities Research Center and Department of Psychiatry and Biobehavioral Sciences, David Geffen School of Medicine at UCLA, Los Angeles, CA

[3]Department of Neurology, David Geffen School of Medicine at UCLA, Los Angeles, CA

[4]UCLA Brain Tumor Imaging Laboratory (BTIL), Department of Radiological Sciences, David Geffen School of Medicine at UCLA, Los Angeles, CA

[5]Department of Neurobiology and Behavior, UCI School of Biological Sciences, Irvine, CA

[6]Department of Pathology, David Geffen School of Medicine at UCLA, Los Angeles, CA

[7]Department of Neurosurgery, Hokuto Social Medical Corporation, Hokuto Hospital, Hokuto, Japan

[8]Center for Translational Neuromedicine, University of Rochester Medical Center, Rochester, NY

[9]Center for Translational Neuromedicine, University of Copenhagen Faculty of Health and Medical Sciences, Copenhagen, Denmark

[10]Departments of Pediatrics and Molecular and Medical Pharmacology, David Geffen School of Medicine at UCLA, Los Angeles, CA

*These authors contributed equally to this work

[#]These authors jointly supervised this work

Corresponding Authors

Harley Kornblum, M.D., Ph.D.

NRB Room 375D, UCLA

635 Charles E. Young Drive South

Los Angeles, CA 90095

hkornblum@mednet.ucla.edu

310-794-7866

Abstract

Both therapy for and molecular investigations into high-grade glioma largely focus on the contrast-enhancing (CE) portion of the tumor. However, given the invasive nature of glioma, residual tumor cells responsible for recurrence exist in the peripheral, non-enhancing (NE) region. Single-cell/single-nucleus RNA-sequencing and subsequent bioinformatics analyses offer a flexible and scalable framework that allows powerful examination of tumor and non-tumor cell subpopulations across various contexts. In this study, we used pre-operative magnetic resonance images to prospectively identify biopsy targets in the CE region and NE sites that lie 0.5-2.0 cm beyond the CE edge from multiple pathologically and molecularly distinct recurrent high-grade gliomas and leveraged single-nucleus RNA-sequencing to generate over 30,000 individual RNA profiles. We analyzed multiple glioma cellular states, non-malignant cell types, and cell-cell interaction patterns, all of which revealed both conserved and patient-specific features. Recurrent gliomas recapitulate the previously reported cellular heterogeneity of primary gliomas. Systematic comparison of the CE and NE regions identified altered composition of malignant and non-malignant cell compartments, as well as cell type- and patient-specific differences in gene expression and pathway activation profiles. We established that NE regions up to 1.5 cm beyond the CE edge contain up to 60% infiltrating malignant cells, of which a significant subset are actively proliferating. These NE glioma cells are preferentially in OPC-like and NPC-like rather than MES-like cellular states. NE cells have altered gene expression patterns, with specific upregulation of certain genes like *DGKB* and *OPHN1* relative to CE regions. We built an integrated atlas of cell-cell communication networks among malignant and non-malignant subpopulations in the two regions of glioma and identified a significantly rewired connectome in the NE regions of all tumors. With respect to tumor-immune interactions, NE regions had decreased numbers of T cells and myeloid cells, along with decreased HLA:CD8 signaling between glioma and immune cells, suggesting decreased immune detection and cell mediated immunity. Furthermore, our findings suggest glioma cells in NE regions maintain interactions with non-malignant neural tissue. Overall, we characterize the NE region in all pathological subtypes of recurrent high-grade glioma and identify possible mechanisms driving progression and recurrence, as well as areas of future therapeutic study.

Introduction

The intervention that contributes most to overall survival in adult glioma remains surgical removal of tumors[12]. The current surgical standard of care is imaging-based resection of the contrast-enhancing (CE) region as depicted by gadolinium contrast-enhanced T1-weighted magnetic resonance imaging (MRI)[3], where increased extent of resection[4] and low post-surgical residual enhancing disease has been shown to be correlated with improved survival[5]. However, despite total resection of the CE region, high-grade gliomas invariably recur, and this most commonly occurs the edge of the resection cavity[6].

Treatment options for recurrent malignant glioma include repeat resection with adjuvant molecular therapy[7–9] and/or immunotherapy[10]. Given the modest efficacy in randomized trials, further study into treatment for recurrent glioma is needed. Strategies for molecularly targeted therapy for recurrent glioma have largely been developed by studying bulk RNA or protein expression from cell lines or clinical surgical specimens, which, as described above, derive from the CE portion of the tumor. This strategy 1) fails to account for cellular heterogeneity and 2) ignores the true targets of adjuvant therapy for recurrent glioma: the residual cells beyond the CE region that are not resected. While more recent studies have utilized single cell sequencing to study intratumoral heterogeneity[11–17], they have largely focused on single samples from CE regions, yielding limited insight about cells beyond the CE region and their clinical relevance. Furthermore, given the importance of tumor-immune interactions and the promise of immunotherapy in recurrent glioma[10], an understanding of the immune landscape in recurrent glioma is needed.

In this study, we prospectively sample CE regions and tissue beyond the enhancing edge (non-enhancing, "NE") from six recurrent high-grade gliomas: four grade 4 IDH-wildtype glioblastomas, one grade 4 IDH-mutant astrocytoma, and one grade 3 IDH-mutant oligodendroglioma. We couple intraoperative neuronavigation-guided targeted biopsy specimens with single-nucleus RNA-sequencing (snRNA-seq) to comprehensively characterize region-specific cellular and molecular features. Our experimental design differs from previous single-cell analyses in glioma in that we leverage prospectively determined positional data to model the spatial landscape of cell populations and utilize multiple biopsy specimens for snRNA-seq to obtain a high number of cells per patient. By studying both malignant and non-malignant cell types, we reveal that the NE region has significant tumor burden, in which there is active proliferation not significantly different from the bulk of the tumor. There are differing proportions of glioma cellular states as well as uniquely dysregulated genes and pathways in NE tumor cells relative

to CE tumor cells. The NE regions have lower levels of non-tumor immune cells and rewired cell-cell interaction networks, suggesting a dampened immune response in this region. Our focus on the biopathology of high-grade glioma in the NE region, beyond the CE region that is the current target of therapy, identifies specific molecular and immunologic targets for future study and therapeutic development.

Results

Analysis of human recurrent gliomas using single-nucleus RNA sequencing

We prospectively identified biopsy targets using pre-operative MRI in patients undergoing surgery for recurrent high-grade glioma. We chose recurrent glioma given limited single cell analysis on recurrent glioma relative to primary glioma[13]. Each patient had a single previous resection with adjuvant temozolomide and radiation therapy only. We selected two biopsy targets from the contrast-enhancing (CE) region of each tumor and one from the non-enhancing (NE) region, located 5-20mm from the CE edge (Fig. 1a). Clinical pathology and fluorescence in situ hybridization identified six high-grade gliomas (four grade 4 IDH-wildtype glioblastomas, one grade 4 IDH-mutant astrocytoma, one grade 3 IDH-mutant and 1p/19q co-deleted oligodendroglioma) and one low-grade glioma (grade 2 IDH-mutant and 1p/19q co-deleted oligodendroglioma) that we included for comparison. We refer to these tumors as Gr4-GBM, Gr4-AST, Gr3-ODG, and Gr2-ODG, respectively (Table 1)[18]. To analyze these tumors, we performed single-nucleus RNA sequencing (snRNA-seq) of all biopsy specimens, yielding 32,914 individual transcriptomes that passed QC and were included in subsequent analyses (Fig. 1b, c, Supplementary Fig. 1a, b).

Characterization of malignant cells in recurrent glioma highlights intra- and intertumoral heterogeneity

To study malignant cell heterogeneity, we first developed an approach that improves upon previously reported strategies for malignant cell identification[13,16,19]. We combined marker expression, hierarchical relationships across unbiased clusters, and an iterative sequence of single cell copy number alteration (CNA) inference analyses to mitigate the effects of classification issues related to inherent clustering flaws or unclear CNA profiles. Malignant cells (Fig. 1d, Supplementary Fig. 1c, d) were then stratified into four cellular states—astrocyte-like (AC-like), mesenchymal-like (MES-like), neural progenitor cell-like (NPC-like), and oligodendrocyte precursor cell-like (OPC-like)—and cycling vs. non-cycling using the module scoring system reported by Neftel et. al[13] (Fig. 2a, Supplementary Fig. 2a-c). Similar to intratumoral heterogeneity seen in primary gliomas[11–13,19], all four cellular

states were identified in our dataset from CE and NE regions (Fig. 2b). There was significant intertumoral heterogeneity in cellular state composition (Fig. 2c): OPC-like and MES-like proportions varied with tumor type, with OPC-like proportion highest in Gr2-ODG and Gr3-ODG and MES-like cells virtually exclusive to Gr4-GBM and Gr4-AST; AC-like proportion was highest in three of the grade 4 tumors and was higher in Gr3-ODG than Gr2-ODG; NPC-like proportions varied but did not clearly relate to diagnosis; and there was significant heterogeneity among the Gr4-GBMs, with one tumor (Gr4-GBM-4) composed almost entirely of MES-like cells. As with primary gliomas, there was greater intertumoral heterogeneity than intratumoral heterogeneity, which we comprehensively evaluated via Augur[20] using an unbiased machine learning algorithm that measures "separability" of cellular populations based on transcriptomic differences (Fig. 2e). There was also significant heterogeneity in cycling fraction (Fig. 2c): as expected, the proportion of cycling cells was highest in the Gr4-GBMs. NPC-like and OPC-like cells (when present) had the two highest cycling proportions in all tumors and cycling AC-like and MES-like cells were exclusive to the grade 4 tumors (Fig. 2d). We noted that each cellular state had a cycling compartment in the grade 4 tumors that consisted of all four cellular states, suggesting that each cellular state has the potential to initiate tumor recurrence.

Significant tumor burden and altered malignant cell composition in the NE regions of high-grade gliomas

We next used MRI-guided positional information to compare the contrast-enhancing (CE) and T2 hyperintense non-enhancing (NE) regions of Gr4-GBMs (1-3), Gr4-AST, and Gr3-ODG (Gr4-GBM-4 only had CE cells that passed QC and Gr2-ODG was a non-enhancing tumor) (Fig. 3a). We first assessed tumor burden in the NE region by quantifying malignant cell proportions, revealing a significant malignant cell burden present in the NE region in all patients (Fig. 3b, Supplementary Fig. 3a). Given that malignant cells comprised a significant proportion of the NE regions, we sought to model the tumor burden extent on MR imaging. Using tumor cell quantity from three locations in three tumors (Gr3-ODG, Gr4-AST, and Gr4-GBM-1), we applied a quadratic model to extrapolate the distance from the center of the tumor to where the tumor burden would approach 0 (Fig. 3c). This model predicted tumor cell presence 2.26-3.09 cm from the center of the tumor, and a spheroid with this radius was constructed and overlaid on the corresponding pre-operative MR image (Fig. 3d). The predicted tumor edge was clearly well beyond the CE region (by 1.41, 1.45, and 1.59 cm, respectively, but within T2 FLAIR hyperintensity. While the invasion and growth patterns of glioma are complex, with cases of multifocal and distant lesions[21], our data suggest a consistent presence of significant tumor burden immediately surrounding the CE bulk.

With the assumption that cycling cells likely drive tumor progression and recurrence, we compared the cycling fractions between the two regions. The proportion of cycling malignant cells was different in NE vs. CE for each patient, but there was no consistent pattern across patients (Fig. 3f). To characterize cycling via immunohistochemistry, we obtained image-guided biopsies from an additional cohort of 22 patients and analyzed a total of 28 tissue specimens from NE regions and 31 from CE regions (Supplementary Fig. 3c). Quantification of Ki-67 staining showed a wide distribution in both regions, including several NE samples with high % positive Ki-67, but no significant difference between regions ($p=0.0957$; unpaired t-test; Fig. 3g). We also analyzed paired samples from five patients with both regions sampled during the same procedure, and % positive Ki-67 was higher in the NE region of each tumor but was not significantly different overall ($p=0.0875$; paired t-test; Fig. 3h-i). We then asked whether cycling proportion could be a useful prognostic tool and found that cycling fraction in CE (but not NE) was predictive of tumor burden in NE ($p<0.01$). Together, these data indicate a significant level of proliferating tumor cells exist in the NE region, are not resected during surgery, and may be potential culprits of recurrence.

We then examined malignant cell subpopulations across regions and noted significant heterogeneity both in terms of cluster proportions (Supplementary Fig. 3b) and cellular state composition (Fig. 3e). In the Gr4-GBMs, MES-like proportion was lower and OPC-like and NPC-like proportion were higher in the NE regions. In the Gr4-AST, NPC-like and OPC-like proportions were lower and AC-like and MES-like proportions were higher in NE. In the Gr3-ODG, AC-like and NPC-like proportions were lower and OPC-like proportion was higher in NE. We also noted regional differences in cycling tendencies of individual cellular states (Supplementary Fig. 3d). In most of the grade 4 tumors, the cycling fraction was lower in AC-like cells and higher in MES-like cells in the NE regions. In all Gr4-GBMs, OPC-like cells had a lower cycling fraction in the NE region, while the opposite was true in Gr3-ODG and Gr4-AST. However, in all samples the most common cellular state of cycling cells in the NE region were OPC-like and NPC-like cells (Supplementary Fig. 3e). These data suggest significantly altered compositional landscape and proliferative tendencies of malignant cellular states in the NE regions relative to CE regions, these regions are marked by intertumoral heterogeneity, but do generally implicate NPC-like and OPC-like cellular states as the actively cycling cells in the NE region.

Altered gene expression and pathway enrichment profiles in malignant cells from NE regions

To investigate regional changes in malignant cell transcriptomes, we identified differentially expressed genes (DEGs) and pathways in the NE vs. CE regions. We first examined whether there were conserved changes in all malignant cells across patients (Fig. 4a, b, Supplementary Fig. 4a), which uncovered several global differential expression patterns. As expected, the number of significant DEGs generally correlated with the number of cells in the comparison. Interestingly, virtually all comparisons within each individual tumor that identified >5 DEGs were skewed in the same direction, suggesting widespread transcriptional activation (Gr4-GBM-2, Gr4-AST, Gr3-ODG) or repression (Gr4-GBM-1, Gr4-GBM-3) in the NE regions. DEGs were then used as input for gene set enrichment analysis (GSEA) to determine functional implications of transcriptional dysregulation in the NE regions with a combination of databases: Gene Ontology Biological Pathways, Canonical Pathways, Oncogenic Pathways, and Transcription Factor Targets. Conserved DEGs in malignant cells across tumors pointed to 686 significantly altered pathways in NE vs. CE (Benjamini-Hochberg adjusted $p<0.05$) (Supplementary Fig. 4c), with upregulation of pathways related to neuronal and synaptic function in NE and downregulation of gene sets linked to extracellular matrix function, immune response, vascular development, EGFR signaling, and hypoxia.

To identify patient-specific regional differences, we analyzed each tumor individually (Fig. 4a, Supplementary Fig. 4b, d), which revealed a wide range of pathway dysregulation in malignant cells: grade 4 tumors had 483-1143 differentially enriched pathways in NE compared to CE, while Gr3-ODC had only 56. In grade 4 tumors, we noted that higher MES-like fraction and lower OPC-like fraction in CE were both correlated with the number of dysregulated pathways in NE, adding to the link that we identified above between cycling fraction in CE and tumor burden in NE. This suggests a possible regulatory balance between these two malignant states that may influence tumor progression and regional heterogeneity. In Gr4-GBM-3, the tumor with the most dysregulated pathways, neuron-/synapse- related terms were upregulated and platelet function, translation elongation, EGFR signaling, immune function, and cilia motility were downregulated in NE. Gr4-GBM-1 also exhibited upregulation in neuronal pathways, along with downregulation of p53/cell cycle regulation/tumor suppression, differentiation, and ECM, suggesting a more proliferative state in the NE region. In Gr4-GBM-2, ribosome- and translation-related terms were upregulated and immune function, transcription, and MAPK signaling were downregulated in NE. In Gr4-AST, there was upregulation in pathways related to B cell function, angiopoietin, and STK33, which has been linked to tumor migration, EMT, and angiogenesis[22]; downregulation was observed in neuronal and synaptic signaling terms.

Finally, Gr3-ODG had mostly upregulated pathways, most prominently related to ribosome and translation, along with node of Ranvier, likely related to the expansion of the OPC-like state. Together, these findings highlight shared and patient-specific regional differences and identify potential NE-specific biological drivers of tumor invasion and recurrence.

We then examined pathway dysregulation in NE vs. CE of each malignant cellular state using GSEA with conserved DEGs across tumors as input, which revealed that AC-like and MES-like cells had the most differentially enriched pathways (103 and 46, respectively) (Fig. 4c). AC-like cells from NE regions had upregulated neuron-, synapse-, and cell-cell interaction-related pathways and downregulated antigen presentation, signaling via the oncogenic transcription factor CRX, immune response, and translation elongation. Interestingly, MES-like cells were the only malignant population that enriched strongly for specific transcription factor target gene sets, with upregulation in NE of OCT1, HNF3 (FOXA1), and MEF2, all of which are known to promote proliferation in glioma[23,24] (Fig. 4d). On the other hand, MES-like cells in the NE region exhibited downregulation of translation and Slit-Robo signaling, which functions in angiogenesis (via VWF), regulation of micro-vasculature density, and VEGF-induced migration/permeability[25]. These patterns, along with the increased cycling fraction in MES-like cells noted above, suggest that MES-like cells are potentially in a distinct functional state in the NE region, likely existing in a more proliferative and less migratory/vascular-interactive state than in the CE region. OPC-like cells had just one conserved dysregulated pathway, which was upregulation in the node of Ranvier cellular compartment; NPC-like cells had 32 dysregulated pathways, with PI3K complex being upregulated and neuron recognition, p53, and cell-cell adhesion being downregulated in NE. In non-cycling cells, HIF1, lymphocyte immunity, and ECM terms were downregulated in NE, while neuronal and synaptic terms were upregulated. Interestingly, in cycling cells, DNA replication was upregulated, and the transcriptional activator FOXJ2 was downregulated, which may explain the global repression phenotype observed in Gr4-GBM-1 and Gr4-GBM-3.

To complement the gene- and pathway-level comparisons, we comprehensively evaluated the degree of cellular dysregulation by leveraging Augur again to measure “separability” of cell populations, or how well an unbiased machine learning algorithm can learn to accurately predict a cell’s identity (e.g., patient, region, or cellular state) given its transcriptome. Examining regional separability (accuracy in predicting whether a cell came from an NE or CE sample) of each cellular state revealed significant heterogeneity across tumors: the most regionally

separable/different cells were AC-like and/or MES-like in Gr4-GBMs and OPC-like and NPC-like in Gr4-AST and Gr3-ODG. We then asked whether there were statistically significant differences in intertumoral (predicting patient identity) or intratumoral (predicting cellular state) heterogeneity in NE compared to CE by generating null distributions of 500 permutations and comparing observed results to the null for each test. Evaluating intertumoral heterogeneity within each cellular state revealed that AC-like and MES-like cells were significantly more different across patients in CE than in NE (accuracy 0.839 and 0.837 in CE and 0.765 and 0.749 in NE, respectively; permutation test, BH-corrected $p<0.01$ for both; Fig. 4e). No other cellular states were significantly different in NE vs. CE in terms of intertumoral heterogeneity. There were no significant differences in intratumoral heterogeneity (separability of cellular states within each tumor) in NE vs. CE (Supplementary Fig. 4f, center). Similar analyses in cells grouped by cycling status showed more accurate prediction of region, patient identity (in both regions separately, with no significant differences in NE vs. CE; Supp Fig. 4f, left), and cellular state (Supp Fig. 4f, right) in cycling cells than non-cycling cells. Taken together, our gene-, pathway-, and population-level analyses strongly implicate MES- and AC-like populations as drivers of conserved biological dysregulation in the NE region of GBM.

Compositional and transcriptomic changes in the non-malignant cell microenvironment in NE region

We next focused on the tumor microenvironment given its importance in tumor biology and therapeutic development. Using marker expression patterns and hierarchical clustering, we identified astrocytes, oligodendrocytes, excitatory neurons, interneurons, endothelial cells, T cells, microglia, and tumor-associated macrophages (Fig. 5a, Supplementary Fig. 5a). We first examined cell type composition and noted that oligodendrocytes and immune cells comprised the majority of all non-tumor cells. One sample (Gr4-GBM-1) had high levels of non-malignant neurons rather than oligodendrocytes, likely due to the NE biopsy site lying in proximity to gray matter rather than white matter. Comparing the NE and CE regions revealed consistent depletion of T cells and decreased or similar myeloid proportions, pointing to a potentially immune-cold environment at the tumor periphery. Consistent with previous reports[26], macrophage:microglia ratio was higher in the CE regions of all tumors except Gr4-GBM-2. We examined global and cell type-specific regional transcriptomic differences by identifying DEGs in NE vs. CE in the integrated dataset (Fig. 5c, Supplementary Fig. 5b). Excitatory neurons and oligodendrocytes had the highest DEG proportion (66% and 54%, respectively, of all genes expressed in at least 5% of cells) (Fig. 5c). As with malignant cell populations, the DEG burden correlated with the number of cells in each cell type. In neurons, we observed upregulation of oxidative phosphorylation and translation terms and

downregulation of neuron- and synapse-related terms, as well as excitatory neuron-specific downregulation of endothelin signaling, in NE. T cells similarly had downregulated neuron-and synapse-related terms in NE. Evaluation of microglia demonstrated upregulation in metabolism and downregulation in immune function in NE, with macrophages interestingly exhibiting the opposite trend. Astrocytes had upregulated HSF1 and oxidative phosphorylation and downregulated receptor-mediated endocytosis and vascular wound healing in NE. Oligodendrocytes also had upregulated HSF1 and downregulated translation-related terms. Endothelial cells exhibited upregulation in protein folding, collagen crosslinking, vessel development, and CD40, and downregulation in translation and neuron migration in NE (Fig. 5d).

We identified several overlapping themes across the malignant and non-malignant compartments of the NE regions. Neuronal pathways were downregulated in T cells and both neuronal subtypes but were upregulated in malignant populations. Multiple OCT1 terms were downregulated in interneurons and excitatory neurons but upregulated in macrophages and MES-like malignant cells. EGFR signaling was downregulated when all malignant cells were combined and when all non-malignant cells were combined. Finally, many genes and pathways linked to vascular function were dysregulated in NE: Robo signaling was downregulated in oligodendrocytes, T cells, and MES-like cells, but upregulated in neurons, and Robo/VEGF crosstalk was downregulated in oligodendrocytes. Furthermore, VEGF signaling was downregulated overall. VEGFA expression was downregulated in macrophages; multiple VEGF ligands were downregulated in oligodendrocytes and macrophages, and multiple VEGF and ANGPT ligands were upregulated in excitatory neurons, along with VWF and PTN. Finally, proteins involved in blood-brain barrier (CLDN11, PDGFRb) were upregulated. These patterns implicate cell type-specific pathway dysregulation that appears to converge on a limited number of themes, including vascular function, metabolism, and neuronal function. Moreover, increased tumor burden and associated immune response in the CE region may stress non-malignant, non-immune cells and lead to a breakdown of normal function, including maintenance of vascular integrity, which in turn may explain leakage of gadolinium from affected blood vessels and therefore contrast enhancement in this region[27].

Cell-cell communication networks in the NE region exhibit functional re-wiring and altered information flow

Crosstalk between malignant cells and normal cells is a hallmark feature of cancer and is critical to tumor growth, invasion, and recurrence[28–31] .To analyze cell-cell interaction (CCI) networks, we utilized CellChat[32], which uses a

comprehensive database of ligand:receptor interactions (Supplementary Fig. 6a) and performs quantitative inference and analysis of intercellular communication via network analysis, pattern recognition, manifold learning, and quantitative contrast approaches. We first built a CCI atlas for each tumor to examine general principles of cellular communication. Each of the four grade 4 gliomas that yielded both NE and CE transcriptomes was analyzed separately, with malignant and non-malignant cells combined. We identified between 112-145 putatively active CCI pathways in each tumor (Supplementary Fig. 6b, c) out of 223 total pathways in the database. A total of 154 unique pathways were identified among the dataset; while there was at least one pathway exclusive to each patient, the majority (95) were detected in all tumors. The putative connectome of each tumor had a rich network structure that involved both paracrine and autocrine communication among cell types (Fig. 6). We then performed differential analysis to identify shared and patient-specific regional differences between NE and CE. For each tumor, the NE and CE regions were analyzed separately and compared with each other using only the cell types present in both regions. Overall communication strength was higher in the NE regions of Gr4-GBM-2, Gr4-GBM-3, and Gr4-AST and the CE region of Gr4-GBM-1 (Fig. 6). Assessing individual cell types identified several patterns. The most and least dysregulated cell types in NE were astrocytes and immune cells, respectively. In each tumor, the cell type with the largest regional difference in sending communication was also the cell type with the largest change in receiving communication, suggesting coordinated regional variation in both ligands and receptors in that cell type. In all tumors, glioma-to-neuron (when present) and glioma-to-oligodendrocyte signaling was increased in NE. However, signaling in the reverse direction (from neurons and oligodendrocytes to glioma cells) correlated with overall strength of signaling; these interactions were stronger (or weaker) in NE in the tumors that had increased (or decreased) overall signaling in NE. In all Gr4-GBMs, autocrine signaling among glioma cells (i.e., glioma-to-glioma) and among astrocytes (when present) was decreased in NE. Finally, in each tumor, the cell type exhibiting the largest increase in paracrine signaling *received* from glioma cells in NE was the same cell type that had the largest increase in paracrine signaling *sent* to immune cells in NE, pointing to a possible 3-way network (i.e., glioma-to-X-to-immune) that may influence immune detection/regulation in the NE region (X = oligodendrocytes in Gr4-GBM-1 and Gr4-GBM-2, neurons in Gr4-GBM-3, and astrocytes in Gr4-AST).

To identify specific CCI pathways driving regional heterogeneity, we used two pathway-level metrics: functional re-wiring (changes in major sender/receiver cell types and directionality of communication) and altered information flow (changes in overall amount of signaling). For each tumor, we identified the most functionally re-wired

signaling pathways in NE vs. CE via joint manifold learning and classification of the inferred communication networks based on their functional similarity (Supplementary Fig. 7). This revealed MHC-I as the only pathway shared among the top functionally re-wired pathways in all tumors, while four pathways previously implicated in glioma—SEMA5, ANGPTL, FGF, and Activin—were each among the top hits in all but one tumor. Examining the specific cell types and ligand-receptor pairs driving this MHC-I dysregulation revealed that HLA:CD8 signaling from glioma cells to immune cells was absent or markedly decreased in the NE regions of all tumors (Fig. 7). Given that HLA downregulation by tumor cells is a mechanism of escaping T cell attack [33], this finding highlights an important regional difference in glioma-immune interactions that may facilitate glioma invasion and recurrence. In terms of altered information flow between NE and CE, 52-69 pathways were identified as significantly different in each tumor (Supplementary Fig. 7). Overlapping these lists revealed three immune-related (CD30, TRAIL, CD40) and two angiogenesis-related (HH, VEGF) pathways that were dysregulated in all tumors (Fig. 7b). After separating the CE- and NE-enriched pathways, we noted significantly more overlap in CE-enriched pathways (9 shared among three tumors, primarily immune- and angiogenesis-related) than NE-enriched pathways (1 shared among three tumors), suggesting a conserved pattern of CCI inhibition in NE that is driven by immune- and angiogenesis-related signaling. Finally, we identified patient-specific regional signatures using the same two metrics. The most functionally re-wired pathways in each tumor were ncWNT (Gr4-GBM-1), NECTIN (Gr4-GBM-2), PTN (Gr4-GBM-3), and SEMA5 (Gr4-AST), each with clear regional differences in cell type and ligand:receptor contributions (Fig. 8). In terms of information flow, each tumor had several signaling pathways that were only detected in CE or NE (Supplementary Fig. 7), the strongest of which were CD6 (CE) and NPNT (NE) in Gr4-GBM-1, CD6 (CE) and IL16 (NE) in Gr4-GBM-2, IFN-I (CE) and IL6 (NE) in Gr4-GBM-3, and HH (CE) and LIFR (NE) in Gr4-AST (Fig. 8). Together, these findings highlight global and cell type-specific dysregulation in cellular communication in the NE regions and identify potential drivers of regional variation in immune and vascular function.

Discussion

In this study, we leveraged single-nucleus RNA sequencing and MRI-guided biopsy target selection to dissect spatial relationships between and within tumor and non-tumor cells in recurrent glioma. We used stringent image guidance to obtain specimens with quantifiable localization. Using nuclear sequencing and strict quality control measures, we were able to analyze on average ~4800 cells per tumor as well as ~1400 tumor cells from the NE

region, an improvement on previous glioma sequencing studies that report either on CE alone or with few cells recovered from the NE region[26,34]. We then characterized the cellular and transcriptomic landscapes of the different tumor regions as described by clinical MRI.

Our study takes advantage of two unique characteristics: 1) inclusion of multiple WHO designations of high-grade glioma[18] and 2) examination of recurrent glioma. We compared the different glioma subtypes using a cellular state model previously used in single-cell analyses. Described in Neftel et al.[13], glioma cellular states were established by identifying gene networks that drive intratumoral heterogeneity in a large cohort of patients, and each state is thought to biologically parallel a normal human cell type (AC-like cells = astrocytes, MES-like = mesenchymal origin, NPC-like = neural progenitors, OPC-like = oligodendrocyte precursors)[13]. We found that the proportions of glioma cellular states correlated with pathological diagnosis, as AC-like and MES-like compartments were expanded in tumors with higher WHO grade. These differences parallel 1) imaging findings (presence of contrast enhancement and necrosis), 2) pathologic differences (neovascularization, invasion, and necrosis), and 3) survival differences among gliomas. The Gr4-AST subtype fit nicely within this context, with cellular state proportions and clinical outcomes falling between Gr3-ODG and Gr4-GBM. We hypothesize that the imaging, pathological, and clinical differences in glioma may be driven by biological heterogeneity due to different cellular state compositions.

We exclusively studied recurrent tumors to examine the similarities and differences on a single-cell level between recurrent glioma and the extensively studied primary glioma. We show that in recurrent high-grade gliomas, tumor biology is remarkably similar to primary gliomas[13,14,19], including the presence of all four malignant cellular states[13] that are more different across than within tumors and whose proportions vary across tumors. In addition, the cycling tendencies of the different cellular states are conserved in recurrent tumors relative to the data from studies on primary glioma[13,15]. Recurrent glioma may be recapitulating a tumor quite similar to its primary. In fact, it may be that “recurrent glioma” is a misnomer; given that the surgical standard of care is maximal safe resection of the CE region of tumor[2], “recurrent glioma” may actually be the natural progression of residual glioma cells left in the infiltrative NE regions surrounding the resection cavity.

With this in mind, we focused on the NE regions by taking MRI-guided samples of these areas during surgery. We confirmed using single-nucleus sequencing that in all recurrent high-grade gliomas (Gr4-GBM, Gr4-AST, Gr3-ODG) there was significant tumor burden beyond the CE region. Our model predicted that cells may exist up to 1.5

cm beyond the CE edge. NE regions had similar levels of cycling cells to the CE region, suggesting these areas are active regions of growth. Of these cycling cells in the NE region, multiple malignant cellular states were proliferating and thus each glioma cellular state may have the potential to drive progression. Interestingly, we found that higher cycling fraction in CE was associated with higher tumor burden in NE, and that the cellular state linked to each pathologic designation (MES in Gr4-GBM, OPC in Gr3-ODG) tended to be the cellular state with the highest cycling fraction in the NE region of those tumors. We found strong differences between the proportion of cellular states in NE and CE regions that are consistent with previous findings in primary glioma: Minata et al.[35] identified higher MES-like cells in CE regions and higher NPC-like cells in NE regions, and Daramanis et al. identified increased proliferation and decreased angiogenesis in NE regions[26]. We saw that NPC-like and OPC-like cells were more abundant in both the low-grade, non-enhancing tumor and in NE regions of high-grade tumors, suggesting potential relationships between cellular states and MRI findings (NPC-/OPC-like cells with non-enhancing characteristics, MES-/AC-like cells with contrast-enhancing characteristics). Overall, our findings add to previous studies implicating the NE region as an area of significant tumor burden characterized by actively proliferating cells and expanded NPC-/OPC-like glioma cellular states relative to the CE region.

Gene- and pathway-level comparisons between the CE and NE regions highlight the large degree of heterogeneity in molecular dysregulation across tumors, both in terms of overall magnitude of dysregulation and which functional networks are implicated. Interestingly, we observed a consistent direction of differential expression within each tumor when analyzing individual subpopulations, suggesting that the upstream drivers of transcriptomic dysregulation are shared or coordinately regulated across malignant cell groups. Importantly, GSEA only considers the rank order of the input genes and is thus not influenced by the number of genes that reached statistical significance in the differential expression analysis. Thus, unlike DEGs, the number of significantly dysregulated pathways is a robust indicator of true changes in biological function, suggesting significantly more functional divergence between the NE and CE regions in grade 4 tumors. Examining GSEA within each tumor identified patient-specific regional differences in several biological domains previously implicated in glioma, namely neuronal/glial function, proliferation, vascular function, immune response, ECM, and metabolism. This differential analysis highlights both common and patient-specific themes related to aberrant molecular and cellular function driven by tumor burden.

The large degree of biological difference between the CE and NE regions prompted us to ask whether we can identify the cell populations driving specific changes. Overall, MES-like and AC-like cells exhibited more pathway dysregulation and transcriptional "separability" between regions than OPC-like and NPC-like cells. Regional pathway enrichment varied considerably across cell states. Compared to the CE region, AC-like cells in NE appeared to function more like normal astrocytes, with upregulation in gene sets related to neuronal/synaptic function and downregulation in translation, immune response, and CRX signaling. Similarly, OPC-like malignant cells in the NE region had upregulation in the node of Ranvier cellular compartment. NPC-like cells in NE appeared to function more like proliferative cells, with upregulation in PI3K and downregulation in p53, but it is unclear whether this is more similar to normal progenitor behavior or tumorigenic proliferation. These data suggest malignant cell types exhibit different biology in CE and NE regions with more conservation of presumed normal cell type biology in NE regions.

Like most aggressive and invasive cancers, high grade glioma depends on a well-orchestrated attack on the existing normal cell ecosystem, likely involving complex interaction networks among malignant and non-malignant populations. The tumor microenvironment, and especially the immune microenvironment, is of importance in the NE region in regard to immune surveillance and immunotherapy. We found that the NE regions harbored lower T cell proportions than CE regions. Consistent with previous reports in primary glioma[26], we found the immune population predominantly consisted of myeloid (macrophage and microglia) cells. This cell type has been associated with immune suppression and potential decreased response to adjuvant therapy[36]. Using cell-cell communication inference, we see a densely interconnected web of signaling involving all possible pairs of malignant and non-malignant populations. Comparing NE and CE regions identified immune dysregulation as a common theme, with significant enrichment of cell-mediated immunity (CD40, CD86, TNFSF14, BAFF, and TRAIL pathways) in CE regions relative to NE. Furthermore, the only functionally rewired signaling pathway shared among the top hits across tumors was MHC-I, and there was decreased HLA:CD8 signaling from glioma cells to immune cells in the NE regions of all tumors. Vascular dysregulation was another common theme: in NE regions, blood brain barrier signaling were intact, hypoxia pathways were downregulated, and VEGF was downregulated. This suggests an oxygen rich microenvironment where tumor cell burden has not outgrown the vascular supply. In turn, there is no need for creation of VEGF-mediated tumor vessels and compromise of the blood brain barrier. Without these vessels, there is no leakage of gadolinium during MRI and therefore no contrast enhancement. Lastly, we see

significant communication in the NE regions between glioma cells and non-malignant cell populations, including oligodendrocytes and neurons. Interactions with infiltrating glioma cells and neurons have been observed[31], suggesting glioma can infiltrate into areas of brain that are still functional. Overall, the microenvironment of NE regions is much closer to normal stroma than the CE region, with decreased immune response, decreased abnormal microvasculature, and increased communication with normal non-malignant cells.

Taken together, this study presents a thorough quantification and molecular characterization of both malignant and non-malignant cell populations and their functional roles in the NE region of recurrent gliomas. These findings have significant clinical implications. First, the presence of significant tumor burden with actively cycling cells multiple centimeters from the edge of the CE region of tumor suggests that resection of this area, when not involving eloquent areas, may improve outcomes. These regions are often not addressed by surgery (with standard of care of surgery being maximal safe resection of CE regions) or adjuvant radiotherapy (with standard of care being radiation to resection cavity with a 2cm margin). Second, given the inability to resect entire NE regions in many cases due to functional eloquence, these residual NE cells are the most likely culprits of recurrence and therefore should be targeted by adjuvant therapy. The presence of vast cell-, gene-, and pathway- level differences in the NE region compared to CE suggests that improvements in adjuvant therapy should be based on investigation of tissue from NE regions rather than the bulk of the tumor, as is current standard in glioma studies. One limitation to this study is low number of tumors studied in each pathological designation. Furthermore, the specimens from NE region in each tumor were limited to a single site given the need to limit sampling of potential non-pathologic neural tissue. Lastly, while studying recurrent gliomas allowed comprehensive characterization and comparison with previous findings in primary gliomas, certain conclusions are limited in their generalizability.

Regarding potential strategies to target the NE region, we point to specific malignant cell types. The bulk of NE regions consists of NPC-/OPC-like cells. These cells continue to interact with normal neurons and oligodendrocytes but have decreased interactions with immune cell types. Furthermore, lack of contrast enhancement in these areas suggest an active blood-brain-barrier, and no more than 20% are cycling at a given time. Therefore, a majority of these cells may be completely unaffected by adjuvant chemotherapy, immunotherapy, and radiation therapy. These NPC-/OPC-like tumor cells in the NE region differentially express genes (*DGKB*, *OPHN1*) that have been identified in regions just beyond gliomas[37] and associated with tumorigenesis[38]. Designing specific molecular therapy against

these cell types and their specific genetic and molecular drivers is a potential therapeutic strategy. Another strategy may be limiting tumor aggression rather than elimination of all malignant cells. Lower grade gliomas have improved survival, and we find a distinction between glioma cell types and pathological entity. Specifically, AC-like and MES-like cells are associated with more aggressive glioma including their most differentially expressed genes in the NE region (*SPARCL1*[39]), as well as hallmark features of higher-grade glioma – angiogenesis, ECM breakdown, and immune response. We also find an inverse relationship in functional pathways between MES-like and OPC-like cellular states. Therefore, a potential therapeutic strategy to slow glioma progression is to maintain a higher OPC-like:MES-like ratio. Lastly, we show decreased proportions of immune cells and decreased interaction with immune cells in NE regions, suggesting that priming these regions for immune response may help improve the efficacy of immunotherapy. Overall, we highlight a previously understudied population of infiltrating cells that exists outside of the enhancing region on MRI and consists of actively dividing glioma cells that interact with normal brain cells in a relatively immune cold environment and that should be the focus of further clinical and scientific exploration.

Methods

Lead contact and materials availability

Please direct requests for further information and/or resources to Harley Kornblum (hkornblum@mednet.ucla.edu).

MRI-guided biopsy targets in human gliomas

This study was approved by the UCLA IRB #10-000655 and #14-001261. All patients provided informed consent for all medical and surgical procedures and involvement in research studies. Patients referred to UCLA Neurosurgery for intrinsic supratentorial brain tumors underwent 3 Tesla thin-cut pre-operative MRI (3T Siemens Prisma, Siemens Healthcare, Erlangen, Germany) with and without gadolinium contrast (gadopentetate dimeglumine; Magnevist; Bayer HealthCare Pharmaceuticals) according to the international standardized brain tumor imaging protocol [40] within 1 week of surgery. Images of the following sequences were downloaded: T1 three-dimension magnetization-prepared rapid gradient echo (MP-RAGE) with and without contrast. Using AFNI, a software for analysis and visualization of functional magnetic resonance neuroimages[41], three 5mm x 5mm x 5mm spherical biopsy targets were selected per patient by a multidisciplinary team (neurosurgery, radiology, and oncology) based on feasibility and anatomic landmarks in order to minimize surgical inaccuracy from brain shift. Biopsy targets were then transferred to Brainlab Curve (BrainLAB AG, Munich, Germany), a surgical

neuronavigation software, for intraoperative image guidance and tissue acquisition. There was no change to surgical and post-surgical standard of care therapy[42] for all patients. Specimens were immediately fresh frozen for nuclear isolation or paraffin-embedded for immunohistochemistry.

Immunohistochemistry analysis

MRI-targeted biopsy specimens were collected from 22 patients with malignant glioma, yielding 28 specimens from NE regions and 31 from CE regions. Specimens were paraffin-embedded and stained with anti-Ki67 antibody. Image based quantification was done using QuPath[43] to calculate percentage of sample pixels with positive staining. Samples were compared using independent samples t-tests as well as paired samples t-tests in the five patients from whom both CE and NE specimens were acquired.

Single-nucleus RNA sequencing (snRNA-seq) of glioma specimens

Single nuclei were isolated from frozen tumor specimens using iodixanol-based density gradient centrifugation (**ref**) and submitted to UCLA Technology Center for Genomics and Bioinformatics for library preparation and sequencing. Single-nucleus cDNA libraries were generated using the Chromium Single Cell 3' v3 kit (10x Genomics) and sequenced at 600 million reads/library and 2x50 base pairs using the NovaSeq 6000 S2 platform (Illumina). Raw reads were demultiplexed and Cell Ranger (10x Genomics) was used for alignment (human genome GRCh38), filtering, barcode identification, and counting of unique molecular identifiers, resulting in a feature-barcode (i.e., gene-cell) matrix for each biopsy specimen.

SnRNA-seq pre-processing, quality control, and analysis

Feature-barcode matrices were further processed and analyzed individually using the R package Seurat package[44–46] (except as noted below). Functions were run with default parameters except as specified. Genes expressed in fewer than 5 nuclei and nuclei expressing fewer than 500 unique genes were both removed. Specimens with a markedly low average number of unique genes expressed per nuclei were removed from the study. Nuclei with mitochondrial transcript content of 5% or greater or ribosomal transcript content of 2% or greater were removed. Counts were normalized and scaled using `SCTransform`[47]. For each patient, the datasets from all specimens were then integrated using Seurat's canonical correlation analysis to account for technical variation[45]. Dimensional reduction was performed on each patient dataset via principal component analysis (PCA), uniform manifold approximation and projection (UMAP) embedding, and t-distributed stochastic neighbor embedding (t-SNE). Clustering was

performed in each patient dataset using Seurat's default graph-based clustering, and low dimensional plots were generated using the `DimPlot` function. Malignant cells were identified using a custom tool that combines marker expression patterns, hierarchical relationships across unbiased clusters, and an iterative sequence of single-cell copy number alteration (CNA) inference analyses to address problematic cells (i.e., incorrect cluster assignment, noisy or unclear CNA profiles) (see Supplementary Methods). Malignant cells were grouped by cellular state (AC-, MES-, NPC-, or OPC-like) and by cycling status using single-cell gene module scores, as reported by Neftel et al. (ref), and their respective pathway enrichment profiles were identified with enrichR[48–50]. Non-malignant cell types were identified based on marker expression profiles (using a modified tool that provides improved marker visualization) and hierarchical clustering, yielding astrocytes, oligodendrocytes, excitatory neurons, interneurons, endothelial cells, T cells, tumor-associated macrophages, and microglia. The integrated dataset for each patient was then split into malignant and non-malignant datasets, which were processed again as above then integrated across patients. The two resulting datasets (malignant cells from all patients, non-malignant cells from all patients) were then prepared for further analysis by dimensional reduction and Seurat clustering as above. Differentially expressed genes (DEGs) were identified using the Seurat functions `FindMarkers` (within-group) and `FindConservedMarkers` (shared) and visualized using `EnhancedVolcano`. Genes expressed in at least 5% of cells were included, and significance was defined as 10% change with $p<0.05$. Gene set enrichment analysis (GSEA) was performed on DEGs ranked by fold change using the fgsea package with a combination of Gene Ontology Biological Pathways, Canonical Pathways, Oncogenic Pathways, and Transcription Factor Targets[51]. Cell-cell communication analysis was performed using the CellChat package[32] with default parameters except as recommended by the developers in their vignettes.

Acknowledgements

This work was supported by the Dr. Miriam and Sheldon G. Adelson Medical Research Foundation (HIK, RK, SAG); NIH grants P50 CA211015 (HIK, BE, DG, WY, LL), R01 NS121617 (HIK), and F31 MH122205 (KKT); the Broad Stem Cell Research Center (KSP, SDM); and the UC President's Postdoctoral Fellowship Program (AGA).

Legends

Table 1. Clinical and pathological characteristics of glioma samples.

Figure 1. Single nucleus RNA-sequencing analysis of MRI-guided glioma biopsy targets. **(a)** Preoperative targeted MRI: T1 with and without contrast, prospective biopsy targets, and intraoperative (IO) neuronavigation renderings of 2 contrast-enhancing and 1 non-enhancing region in Gr4-AST (grade IV IDH-mutant astrocytoma) and Gr4-GBM-1 (grade IV IDH-WT glioblastoma). **(b)** Glioma single-nucleus RNA-sequencing (snRNA-seq) experimental workflow, created with Biorender.com. **(c, d)** Low dimensional t-distributed stochastic neighbor embedding (t-SNE) plots showing the integrated snRNA-seq dataset with all sequenced nuclei **(c)** and those identified as malignant **(d)**, colored by expression-based clusters (left) or patient identity (right).

Figure 2. Recapitulation of established malignant cellular states in recurrent glioma. (a) Malignant glioma cells classified by cellular state (AC-like, MES-like, NPC-like, and OPC-like) using gene network module scores as described by Neftel et al. (2019). Shown are all malignant cells integrated across tumors and plotted based on relative enrichment among the cellular state meta-modules. **(b)** Top enriched pathways in each cellular state and in cycling cells. **(c)** Visualization and evaluation via ANOVA of intertumoral differences in malignant cell state composition (* indicates FDR<0.05, *** indicates FDR<0.001). **(d)** Proportion of cycling cells detected in each cellular state across patients. **(e)** Cell type prioritization via Augur. Results from training the classifier to predict patient ID given cell state (left) or to predict cell state given patient ID (right), to evaluate inter- and intra-tumoral heterogeneity, respectively, using CE samples.

Figure 3. Characterizing tumor burden and composition in the non-enhancing region. (a) Malignant cells labeled by biopsy region and visualized using t-SNE coordinates. **(b)** Quantification of malignant cell burden (proportion of all cells that are malignant) in the NE vs CE regions of each tumor. **(c)** Tumor burden relative to distance from center of tumor was modeled for the first 3 sequenced tumors by fitting the tumor:non-tumor oligodendrocyte ratio to a quadratic curve (solid line), with the x-asymptote (dotted line) representing predicted distance from the tumor center where tumor burden approaches 0. **(d)** Heatmap of tumor burden based on quadratic formula overlaid on pre-operative MR scan. **(e, f)** Proportion of malignant cellular states **(e)** and cycling cells **(f)** in the NE vs CE regions. **(g, h)** Quantification of immunohistochemistry staining for Ki67 stratified by region of acquisition using non-paired **(g)** and paired **(h)** biopsy samples. **(i)** Representative example of regions of Ki67 staining in enhancing and non-enhancing regions.

Figure 4. Region-specific molecular features of malignant cells in high-grade glioma. (a) Number of upregulated and downregulated differentially expressed genes (DEGs) in NE vs. CE in each tumor and cell group. **(b)** Conserved DEGs across patients. **(c)** Cell state-specific significant hits from gene set enrichment analysis (GSEA) using DEGs conserved across patients (NE vs. CE). **(d)** GSEA results for MES-like cells using conserved DEGs across patients. (e) Cell type prioritization via Augur to assess change in intertumoral heterogeneity within each malignant population in NE vs. CE.

Figure 5. Altered non-malignant cell microenvironment in NE region of high-grade gliomas. (a) t-SNE representation of non-malignant cells labeled by cell type based on marker expression profiles. **(b)** Differential abundance analysis of normal cell types in the NE vs. CE regions. **(c)** Differential expression analysis within cell types, NE vs. CE. Shown are percentage of considered genes (those expressed in >5% of cells) that were found to be differentially expressed. **(d)** Summary of cell type-specific GSEA results using the identified DEGs with a combination of the GO Biological Process, Canonical Pathway, Oncogenic Pathway, and Transcription Factor Target databases. *(Astro = astrocytes, Endo = endothelial cells, ExN = excitatory neurons, InN = interneurons, Mac = macrophages, MG = Microglia, Oligo = oligodendrocytes, T_cell = T cells)*

Figure 6. Regional differences in cell-cell interaction strength at the cell type level. Cell-cell interaction (CCI) patterns were identified using CellChat, and NE and CE regions were compared using differential analysis. Shown are interaction strengths among possible cell type pairs (both paracrine and autocrine signaling) in both CE and NE, along with differential analysis of interaction strengths (red = increase, blue = decrease).

Figure 7. Shared regional differences in network wiring and signaling strength (pathway level). (a) Overlap of dysregulated pathways in NE vs. CE across patients, based on functional re-wiring (i.e., cell type involvement) or quantitative changes (i.e., increased or decreased signaling in NE). Altered information flow refers to quantitative change in either direction (either increased or decreased in NE vs. CE). **(b)** Circle plots showing MHC-I signaling profile in CE and NE of each tumor. (c) Bubble plot showing strength of specific MHC-I ligand:receptor (rows) interaction strengths within each cell-cell interaction (columns).

Figure 8. Top re-wired and quantitatively dysregulated pathways for each patient in NE vs. CE. Visualization of one of the top 3 functionally re-wired pathways in NE vs. CE of each patient (columns). Shown are circle plots reflecting specific paracrine and autocrine signaling strengths in CE and NE (top) and bubble plots indicating specific ligand:receptor and cell:cell pairs mediating the high degree of re-wiring. Also shown are the top CE- and NE-enriched pathways (most quantitatively dysregulated) in each tumor (bottom).

Supplementary Figure 1. Related to Fig. 1. Integrated snRNA-seq dataset with nuclei split by patient identity and colored by cluster; cells projected onto t-SNE **(a)** or uniform manifold approximation and projection (UMAP) **(b)** coordinates. **(c)** Example of copy number alteration analysis using biopsy specimens from Gr4-GBM-3. **(d)** Malignant cells plotted based on 3-dimensional UMAP embedding.

Supplementary Figure 2. Related to Fig. 2. (a) Heatmap depicting expression of top 10 genes across the gene lists reported by Neftel et al. (2019). Rows correspond to genes and columns to cells. Cells are grouped according to cellular state, with cycling cells plotted separately. A random subset of 5000 malignant cells were included. **(b)** t-SNE plot of malignant cells from all tumors colored by cellular state, with cycling cells identified by fitting G1/S and G2/M scores as in Neftel et al. (2019). **(c)** t-SNE plot with MKI67 expression superimposed.

Supplementary Figure 3. Related to Fig. 3. (a) Malignant cells grouped by biopsy region and colored by cluster (left) or grouped by patient identity and colored by biopsy region (right), visualized using t-SNE coordinates. **(b)** Breakdown of expression-based cluster proportions in each region. **(c)** Clinical and pathological characteristics of patients included in immunohistochemistry analyses (**Fig. 4g-i**). **(d, e)** Cross-classification abundance analysis, combining cellular state groups with cycling status.

Supplementary Figure 4. Related to Fig. 4. DEGs in NE vs. CE in the integrated dataset **(a)** and in individual tumors **(b)**. **(c)** GSEA results using all malignant cells and conserved DEGs across patients. **(d,e)** Volcano plots visualizing NE vs. CE differential expression results in each patient **(d)** and cell state **(e)**. **(f)** Cell type prioritization via Augur to assess differences in NE vs. CE in patient ID predictability (i.e., intertumoral heterogeneity) within cycling and non-cycling cells (left) and cell state predictability (i.e., intratumoral heterogeneity) given patient ID (middle) or cycling status (right).

Supplementary Figure 5. Related to Fig. 5. (a) Phylogenetic tree (left) and dot plot (right) showing marker expression patterns across non-malignant cell clusters. **(b, c)** Volcano plots showing results of combined and cell type-specific differential expression analysis, NE vs. CE.

Supplementary Figure 6. Related to Fig 6. (a) Summary of human CellChat interaction database used for analysis. **(b)** Overlap of identified CCI pathways across patients. **(c)** Quantification of pathways that were identified, altered in NE vs. CE (in either direction), CE-enriched, and NE-enriched.

Supplementary Figure 7. Related to Fig. 7. Identification of functionally re-wired **(a, b)** and quantitatively dysregulated **(c)** pathways in NE vs. CE of Gr4-GBM-1. Similar visualization for Gr4-GBM-2 **(d-f)**, Gr4-GBM-3 **(g-i)**, and Gr4-AST **(j-l)**.

References

1. Marko, N. F. *et al.* Extent of resection of glioblastoma revisited: personalized survival modeling facilitates more accurate survival prediction and supports a maximum-safe-resection approach to surgery. *J Clin Oncol* **32**, 774–782 (2014).
2. Brown, T. J. *et al.* Association of the Extent of Resection With Survival in Glioblastoma: A Systematic Review and Meta-analysis. *JAMA Oncol* **2**, 1460–1469 (2016).
3. Wen, P. Y. & Kesari, S. Malignant gliomas in adults. *N. Engl. J. Med.* **359**, 492–507 (2008).
4. Sanai, N., Polley, M.-Y., McDermott, M. W., Parsa, A. T. & Berger, M. S. An extent of resection threshold for newly diagnosed glioblastomas. *J. Neurosurg.* **115**, 3–8 (2011).
5. Ellingson, B. M. *et al.* Validation of postoperative residual contrast-enhancing tumor volume as an independent prognostic factor for overall survival in newly diagnosed glioblastoma. *Neuro Oncol* **20**, 1240–1250 (2018).
6. Bette, S. *et al.* Retrospective Analysis of Radiological Recurrence Patterns in Glioblastoma, Their Prognostic Value And Association to Postoperative Infarct Volume. *Sci Rep* **8**, 4561 (2018).
7. Erdem-Eraslan, L. *et al.* Identification of Patients with Recurrent Glioblastoma Who May Benefit from Combined Bevacizumab and CCNU Therapy: A Report from the BELOB Trial. *Cancer Res* **76**, 525–534 (2016).
8. Taal, W. *et al.* Single-agent bevacizumab or lomustine versus a combination of bevacizumab plus lomustine in patients with recurrent glioblastoma (BELOB trial): a randomised controlled phase 2 trial. *Lancet Oncol.* **15**, 943–953 (2014).
9. Brandes, A. A. *et al.* AVAREG: a phase II, randomized, noncomparative study of fotemustine or bevacizumab for patients with recurrent glioblastoma. *Neuro Oncol* **18**, 1304–1312 (2016).
10. Cloughesy, T. F. *et al.* Neoadjuvant anti-PD-1 immunotherapy promotes a survival benefit with intratumoral and systemic immune responses in recurrent glioblastoma. *Nat Med* **25**, 477–486 (2019).

11. Patel, A. P. *et al.* Single-cell RNA-seq highlights intratumoral heterogeneity in primary glioblastoma. *Science* **344**, 1396–1401 (2014).
12. Venteicher, A. S. *et al.* Decoupling genetics, lineages, and microenvironment in IDH-mutant gliomas by single-cell RNA-seq. *Science* **355**, (2017).
13. Neftel, C. *et al.* An Integrative Model of Cellular States, Plasticity, and Genetics for Glioblastoma. *Cell* **178**, 835-849.e21 (2019).
14. Tirosh, I. *et al.* Single-cell RNA-seq supports a developmental hierarchy in human oligodendroglioma. *Nature* **539**, 309–313 (2016).
15. Weng, Q. *et al.* Single-Cell Transcriptomics Uncovers Glial Progenitor Diversity and Cell Fate Determinants during Development and Gliomagenesis. *Cell Stem Cell* **24**, 707-723.e8 (2019).
16. Wang, L. *et al.* The Phenotypes of Proliferating Glioblastoma Cells Reside on a Single Axis of Variation. *Cancer Discov* **9**, 1708–1719 (2019).
17. Lan, X. *et al.* Fate mapping of human glioblastoma reveals an invariant stem cell hierarchy. *Nature* **549**, 227–232 (2017).
18. Louis, D. N. *et al.* The 2021 WHO Classification of Tumors of the Central Nervous System: a summary. *Neuro Oncol* **23**, 1231–1251 (2021).
19. Couturier, C. P. *et al.* Single-cell RNA-seq reveals that glioblastoma recapitulates a normal neurodevelopmental hierarchy. *Nat Commun* **11**, 3406 (2020).
20. Squair, J. W., Skinnider, M. A., Gautier, M., Foster, L. J. & Courtine, G. Prioritization of cell types responsive to biological perturbations in single-cell data with Augur. *Nat Protoc* **16**, 3836–3873 (2021).
21. Schaub, C. *et al.* Tumor growth patterns of MGMT-non-methylated glioblastoma in the randomized GLARIUS trial. *J. Cancer Res. Clin. Oncol.* **144**, 1581–1589 (2018).
22. Liu, Y. *et al.* STK33 participates to HSP90-supported angiogenic program in hypoxic tumors by regulating HIF-1α/VEGF signaling pathway. *Oncotarget* **8**, 77474–77488 (2017).

23. Rooj, A. K., Bronisz, A. & Godlewski, J. The role of octamer binding transcription factors in glioblastoma multiforme. *Biochim Biophys Acta* **1859**, 805–811 (2016).

24. Zhang, C., Yang, M., Li, Y., Tang, S. & Sun, X. FOXA1 is upregulated in glioma and promotes proliferation as well as cell cycle through regulation of cyclin D1 expression. *Cancer Manag Res* **10**, 3283–3293 (2018).

25. Guo, S.-W., Zheng, Y., Lu, Y., Liu, X. & Geng, J.-G. Slit2 overexpression results in increased microvessel density and lesion size in mice with induced endometriosis. *Reprod Sci* **20**, 285–298 (2013).

26. Darmanis, S. *et al.* Single-Cell RNA-Seq Analysis of Infiltrating Neoplastic Cells at the Migrating Front of Human Glioblastoma. *Cell Rep* **21**, 1399–1410 (2017).

27. Treiber, J. M. *et al.* Molecular physiology of contrast enhancement in glioblastomas: An analysis of The Cancer Imaging Archive (TCIA). *J Clin Neurosci* (2018) doi:10.1016/j.jocn.2018.06.018.

28. Caspani, E. M., Crossley, P. H., Redondo-Garcia, C. & Martinez, S. Glioblastoma: a pathogenic crosstalk between tumor cells and pericytes. *PLoS One* **9**, e101402 (2014).

29. Venkatesh, H. S. *et al.* Neuronal Activity Promotes Glioma Growth through Neuroligin-3 Secretion. *Cell* **161**, 803–816 (2015).

30. Venkatesh, H. S. *et al.* Targeting neuronal activity-regulated neuroligin-3 dependency in high-grade glioma. *Nature* **549**, 533–537 (2017).

31. Venkatesh, H. S. *et al.* Electrical and synaptic integration of glioma into neural circuits. *Nature* **573**, 539–545 (2019).

32. Jin, S. *et al.* Inference and analysis of cell-cell communication using CellChat. *Nat Commun* **12**, 1088 (2021).

33. Yeung, J. T. *et al.* LOH in the HLA class I region at 6p21 is associated with shorter survival in newly diagnosed adult glioblastoma. *Clin Cancer Res* **19**, 1816–1826 (2013).

34. Gill, B. J. *et al.* MRI-localized biopsies reveal subtype-specific differences in molecular and cellular composition at the margins of glioblastoma. *Proc. Natl. Acad. Sci. U.S.A.* **111**, 12550–12555 (2014).

35. Minata, M. *et al.* Phenotypic Plasticity of Invasive Edge Glioma Stem-like Cells in Response to Ionizing Radiation. *Cell Rep* **26**, 1893-1905.e7 (2019).

36. Li, J. *et al.* PI3Kγ inhibition suppresses microglia/TAM accumulation in glioblastoma microenvironment to promote exceptional temozolomide response. *Proceedings of the National Academy of Sciences* **118**, (2021).

37. Ljubimova, J. Y. *et al.* Gene expression abnormalities in human glial tumors identified by gene array. *Int J Oncol* **18**, 287–295 (2001).

38. Yang, J. *et al.* Circular RNA DGKB Promotes the Progression of Neuroblastoma by Targeting miR-873/GLI1 Axis. *Front Oncol* **10**, 1104 (2020).

39. Gagliardi, F. *et al.* Enhanced SPARCL1 expression in cancer stem cells improves preclinical modeling of glioblastoma by promoting both tumor infiltration and angiogenesis. *Neurobiol Dis* **134**, 104705 (2020).

40. Ellingson, B. M. *et al.* Consensus recommendations for a standardized Brain Tumor Imaging Protocol in clinical trials. *Neuro-oncology* **17**, 1188–1198 (2015).

41. Cox, R. W. AFNI: software for analysis and visualization of functional magnetic resonance neuroimages. *Comput. Biomed. Res.* **29**, 162–173 (1996).

42. Stupp, R. *et al.* Radiotherapy plus concomitant and adjuvant temozolomide for glioblastoma. *N. Engl. J. Med.* **352**, 987–996 (2005).

43. Bankhead, P. *et al.* QuPath: Open source software for digital pathology image analysis. *Sci Rep* **7**, 16878 (2017).

44. Heinemann, J. Cluster Analysis of Untargeted Metabolomic Experiments. *Methods Mol Biol* **1859**, 275–285 (2019).

45. Stuart, T. *et al.* Comprehensive Integration of Single-Cell Data. *Cell* **177**, 1888-1902.e21 (2019).

46. Hao, Y. *et al.* Integrated analysis of multimodal single-cell data. *Cell* **184**, 3573-3587.e29 (2021).

47. Hafemeister, C. & Satija, R. Normalization and variance stabilization of single-cell RNA-seq data using regularized negative binomial regression. *Genome Biol* **20**, 296 (2019).

48. Chen, E. Y. *et al.* Enrichr: interactive and collaborative HTML5 gene list enrichment analysis tool. *BMC Bioinformatics* **14**, 128 (2013).

49. Kuleshov, M. V. *et al.* Enrichr: a comprehensive gene set enrichment analysis web server 2016 update. *Nucleic Acids Res* **44**, W90-97 (2016).

50. Xie, Z. *et al.* Gene Set Knowledge Discovery with Enrichr. *Curr Protoc* **1**, e90 (2021).

51. Liberzon, A. *et al.* Molecular signatures database (MSigDB) 3.0. *Bioinformatics* **27**, 1739–1740 (2011).

Table 1. Clinical and pathological characteristics of glioma samples

Patient	Tumor	Diagnosis	Grade	IDH	FISH
Gr4-GBM-1	TB78	Glioblastoma	IV	WT	PTEN -
Gr4-GBM-2	PT90	Glioblastoma	IV	WT	-
Gr4-GBM-3	PT94	Glioblastoma	IV	WT	-
Gr4-GBM-4	PT95	Glioblastoma	IV	WT	-
Gr4-AST	TB77	Astrocytoma	IV	R132H	EGFR +
Gr3-ODG	TB76	Oligodendroglioma	III	R132H	1p/19q -/-
Gr2-ODG	TB81	Oligodendroglioma	II	R132H	1p/19q -/-

Figure 1. Single nucleus RNA-sequencing analysis of MRI-guided glioma biopsy targets

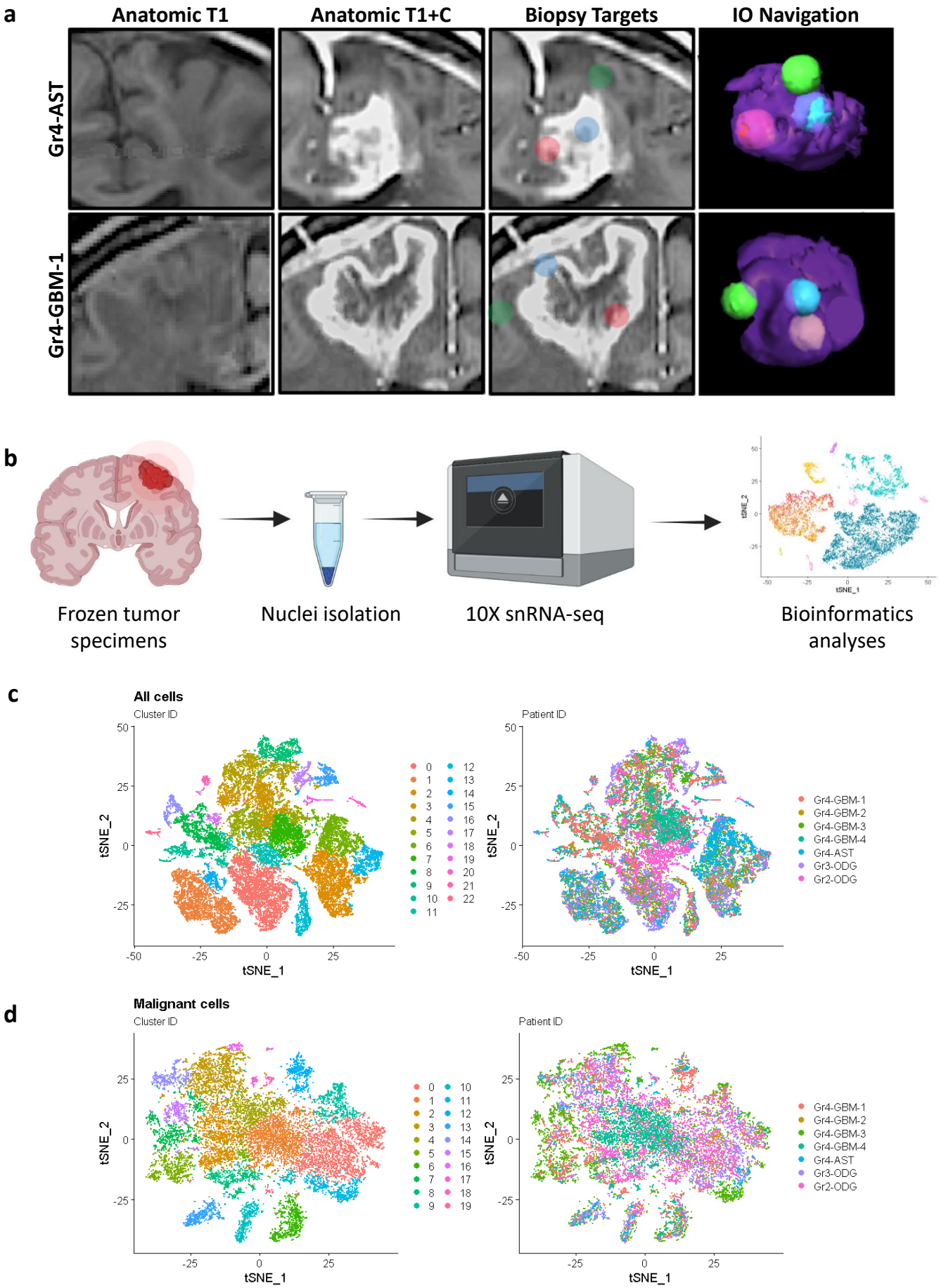

Figure 2. Recapitulation of established malignant cellular states in recurrent glioma

Figure 3. Characterizing tumor burden and composition in the non-enhancing region

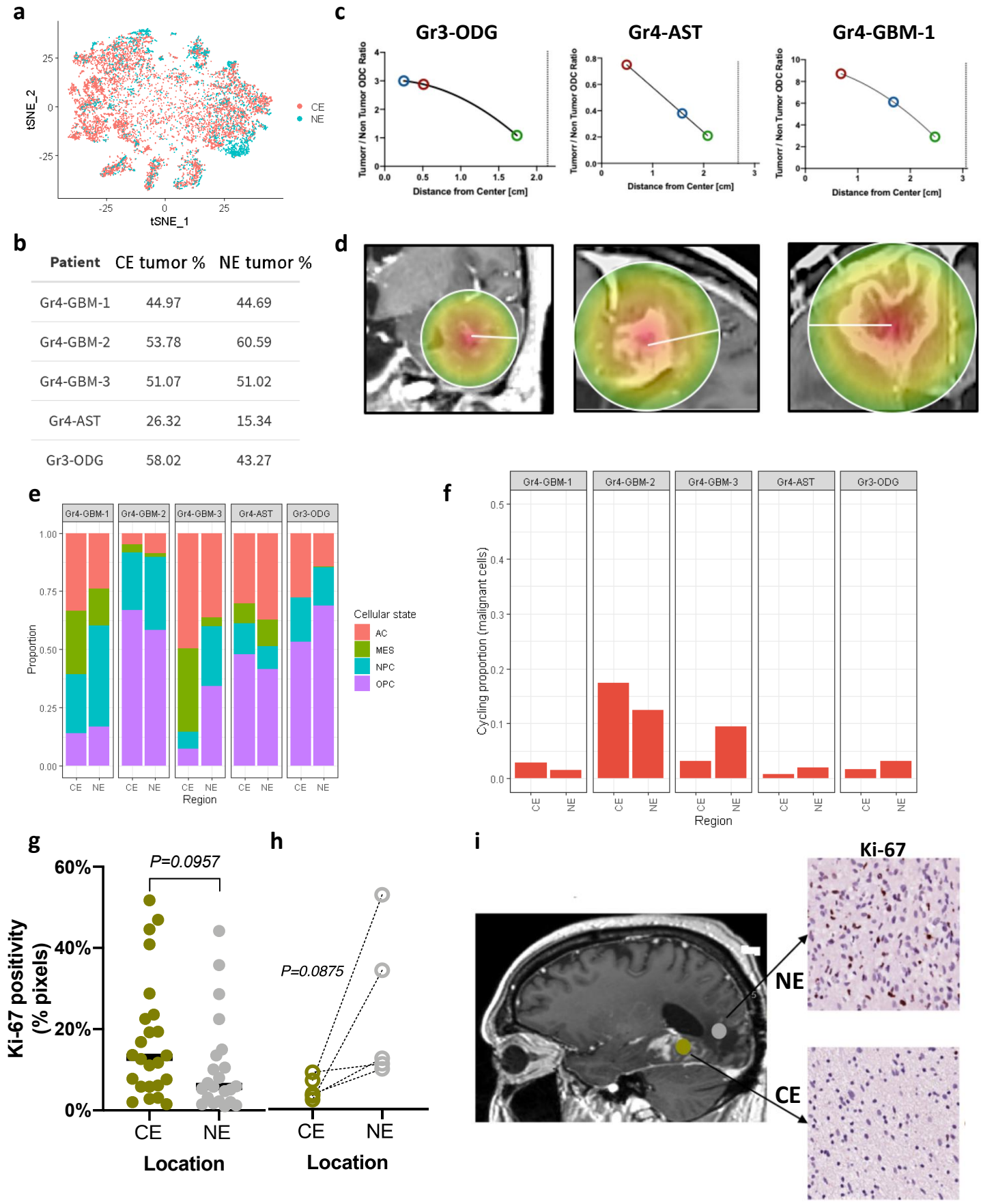

Patient	CE tumor %	NE tumor %
Gr4-GBM-1	44.97	44.69
Gr4-GBM-2	53.78	60.59
Gr4-GBM-3	51.07	51.02
Gr4-AST	26.32	15.34
Gr3-ODG	58.02	43.27

Figure 4. Region-specific molecular features of malignant cells in high-grade glioma

a

Pt	All	AC	MES	NPC	OPC	Cycling
Gr4-GBM-1	↑224 ↓585	↑3 ↓5	↑7 ↓9	↑41 ↓20	↑5 ↓0	↑0 ↓0
Gr4-GBM-2	↑78 ↓43	↑2 ↓0	↑17 ↓0	↑16 ↓6	↑39 ↓21	↑4 ↓3
Gr4-GBM-3	↑1021 ↓2356	↑207 ↓1633	↑8 ↓43	↑50 ↓447	↑80 ↓817	↑10 ↓46
Gr4-AST	↑1105 ↓46	↑6 ↓0	↑0 ↓2	↑0 ↓0	↑289 ↓0	↑0 ↓0
Gr3-ODG	↑530 ↓153	↑41 ↓21	↑0 ↓0	↑37 ↓10	↑377 ↓51	↑0 ↓0

b

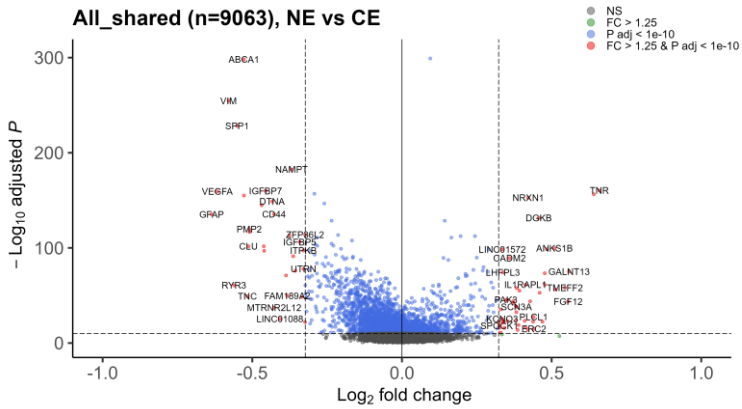

c

State	Total	↑ NE	↓ NE
AC	103	Neuron, synapse, CCI	Immunity, translation, CRX
MES	46	**Proliferation** (TFs: OCT1, HNF3, MEF2), synapse	**Migration, vasculature**, differentiation, translation
NPC	32	PI3K complex	Neuron recognition, p53, cell-cell adhesion
OPC	1	Node of Ranvier	--
Cycling		DNA replication	Transcription (FOXJ2), factor X
Resting		Neuron, synapse	Hypoxia (HIF1), immunity, ECM

e

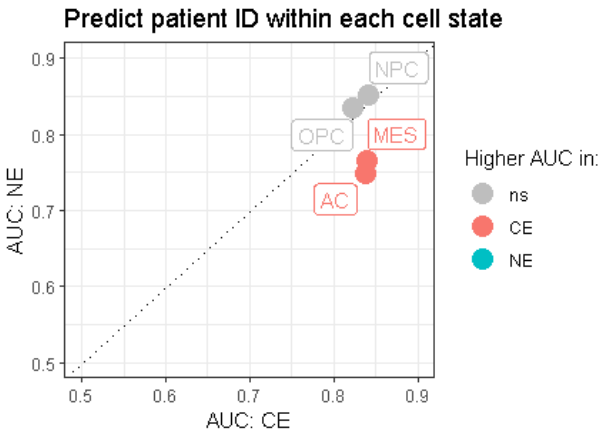

d

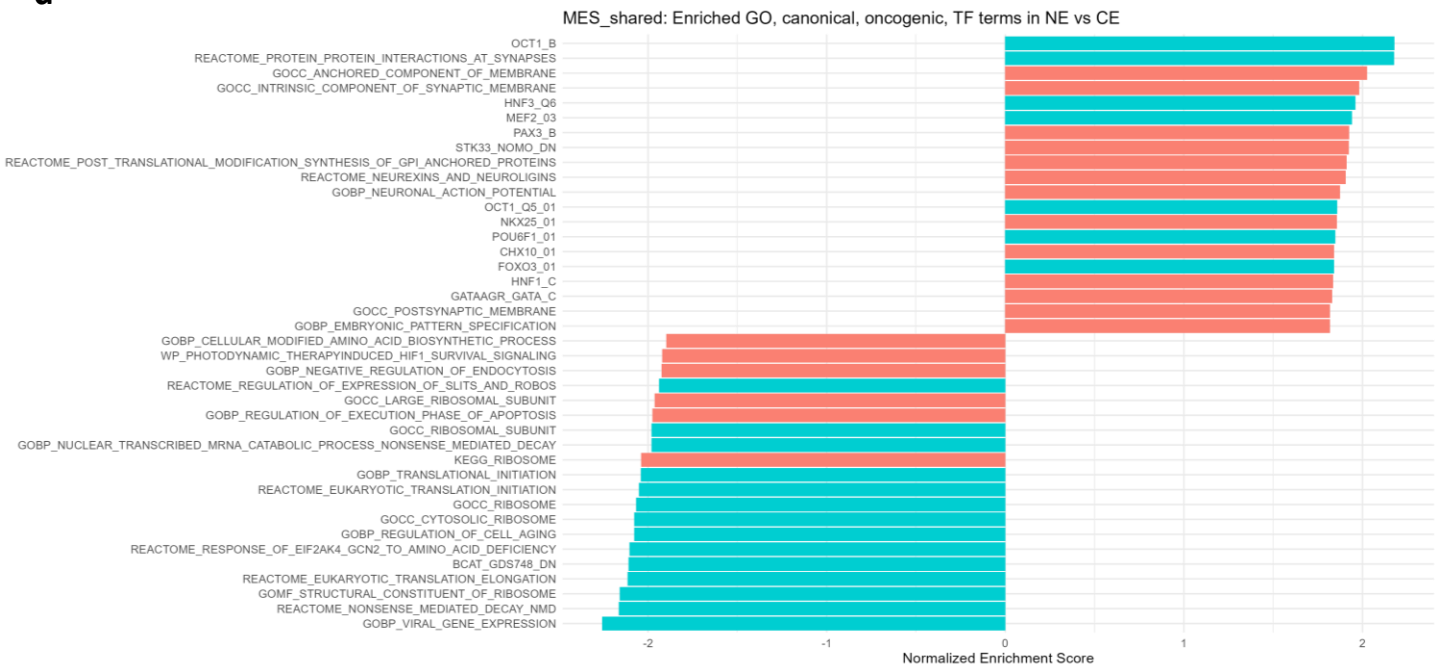

Figure 5. Altered non-malignant cell microenvironment in NE region of high-grade gliomas

a

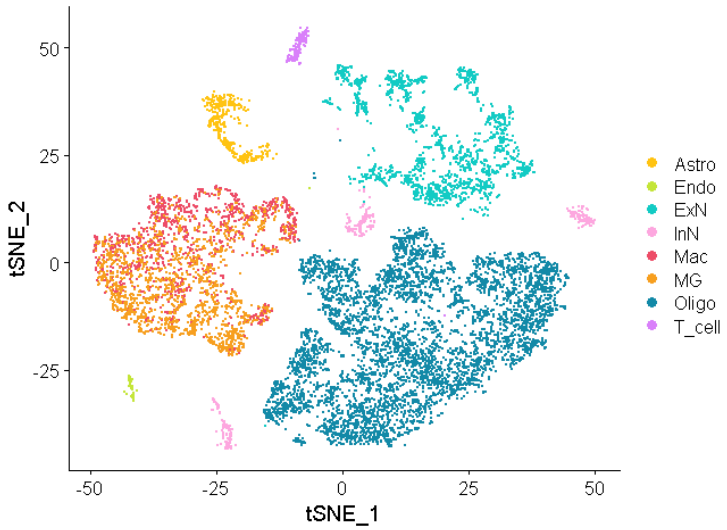

b

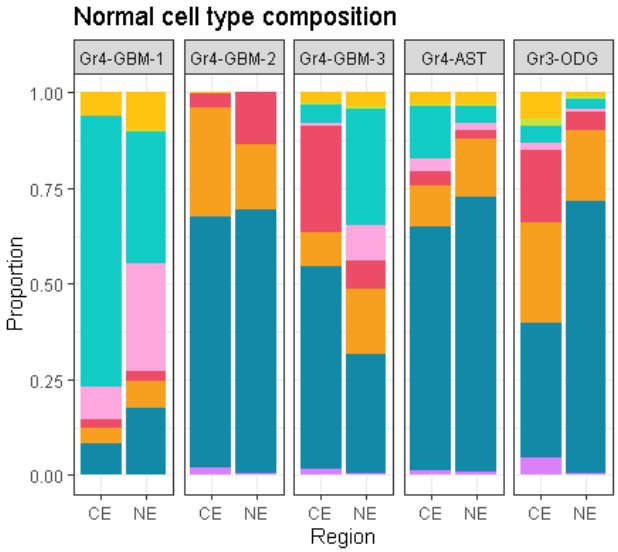

c

Cell type	% DEG*
Ex neurons	66%
Oligo	54%
All others	< 10%

d

State	Total	↑ NE	↓ NE
Oligo	531	HSF1, protein folding	Translation, Slit-Robo
ExN	358	Ox phos, translation	**Neuron, synapse, OCT1, endothelin**
Mac	360	Immunity	Metabolism
InN	343	Ox phos, translation	**Neuron, synapse, OCT1**
MG	170	Metabolism	Immunity
Endo	108	Protein folding, **collagen crosslinking, vascular development, CD40**	Translation, neuron migration
T cell	77	Proteoglycans	**Neuron, synapse**, translation
Astro	34	HSF1, ox phos	Endocytosis, **vascular** wound healing, cAMP

Figure 6. Regional differences in cell-cell interaction strength at the cell type level

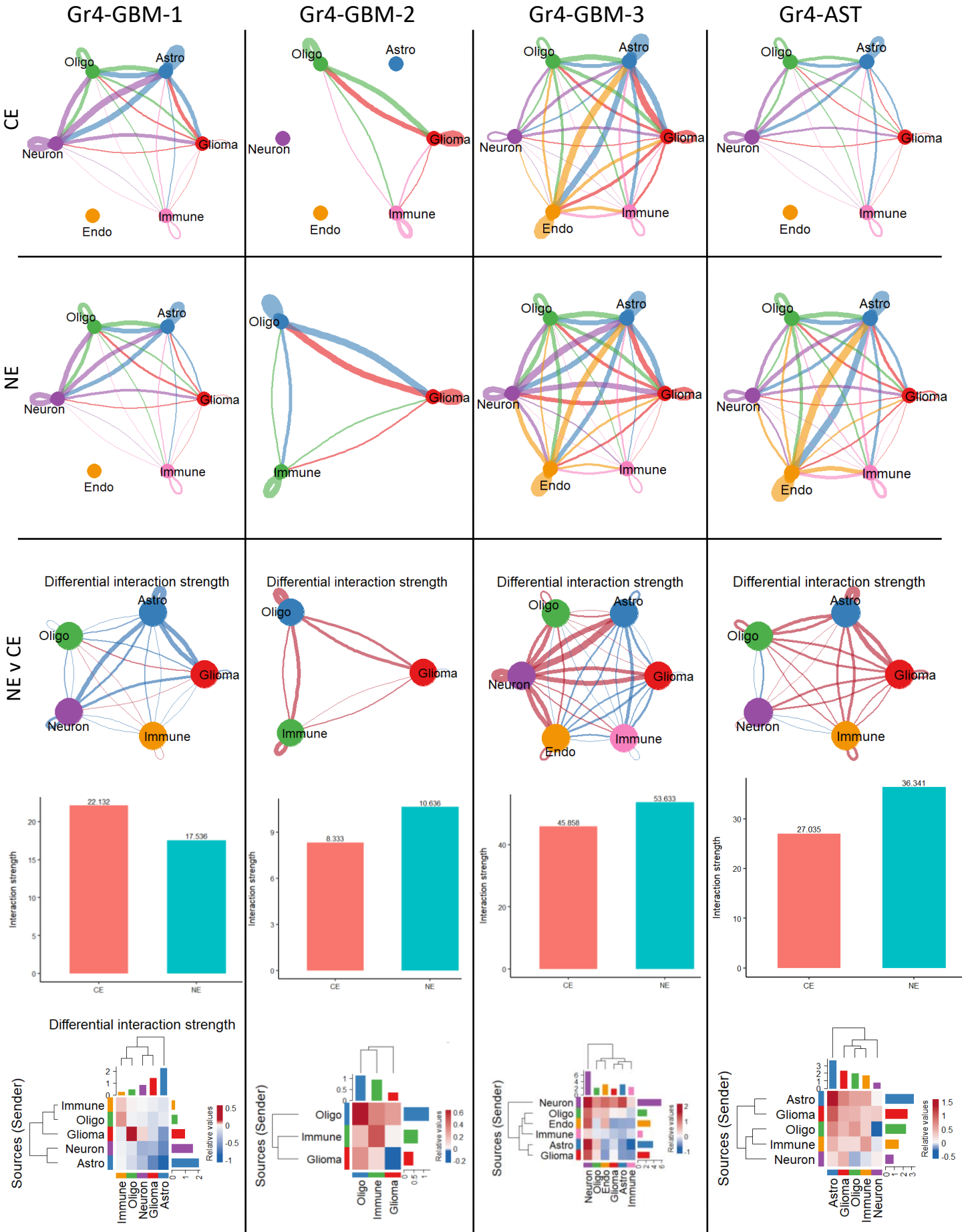

Figure 7. Shared regional differences in network wiring and signaling strength (pathway level)

a

Top 20 functionally re-wired

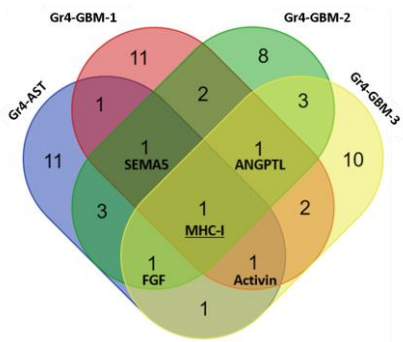

Altered information flow

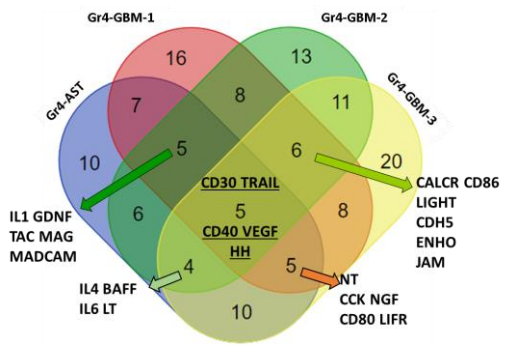

CE-enriched

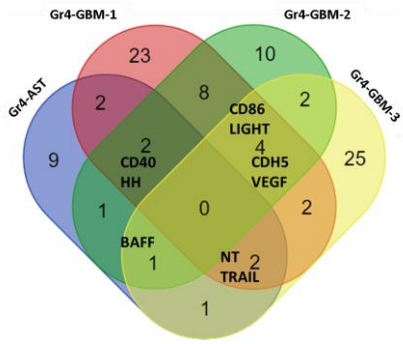

NE-enriched

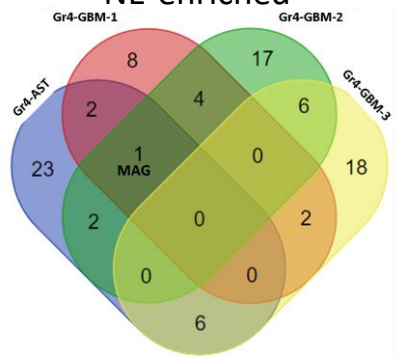

b

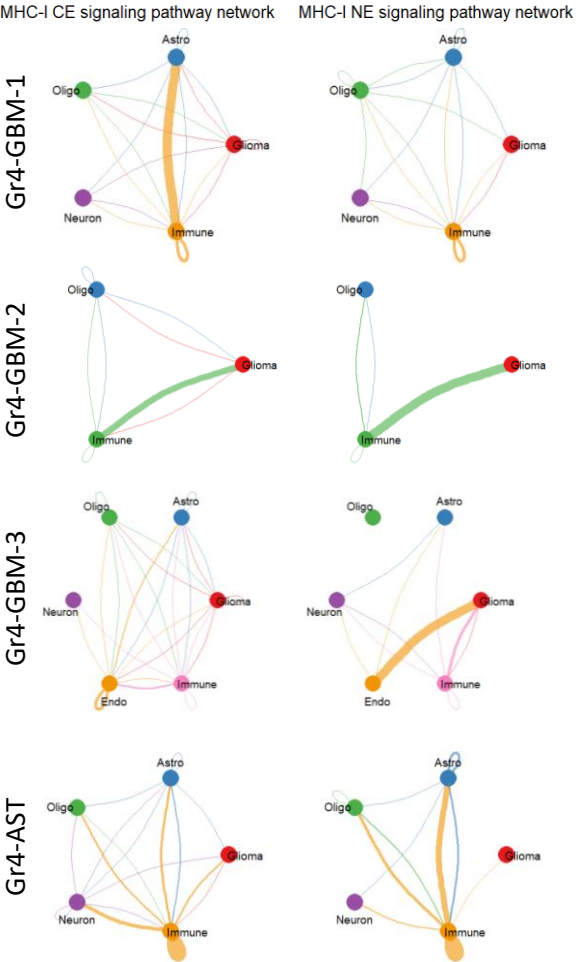

c

Figure 8. Top re-wired and quantitatively dysregulated pathways for each patient in NE vs CE

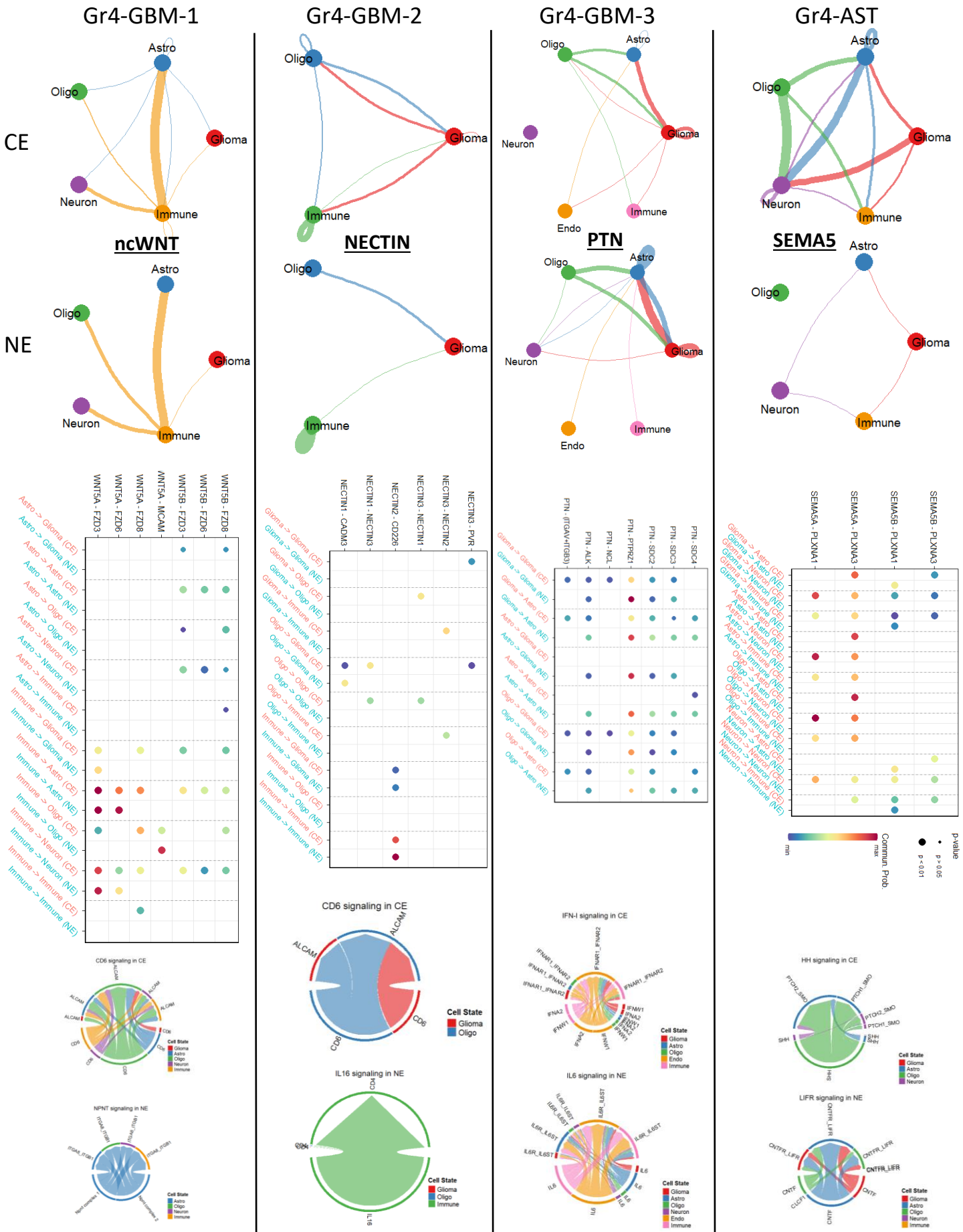

Supplementary Figure 1. Related to Fig. 1

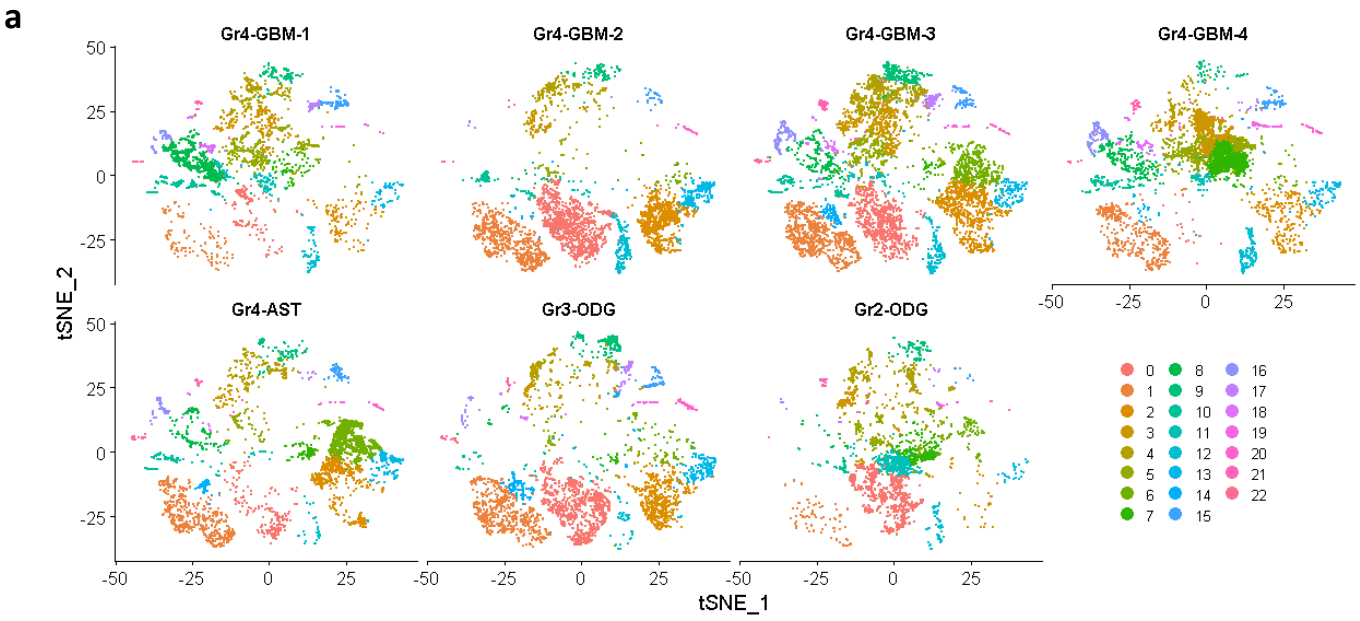

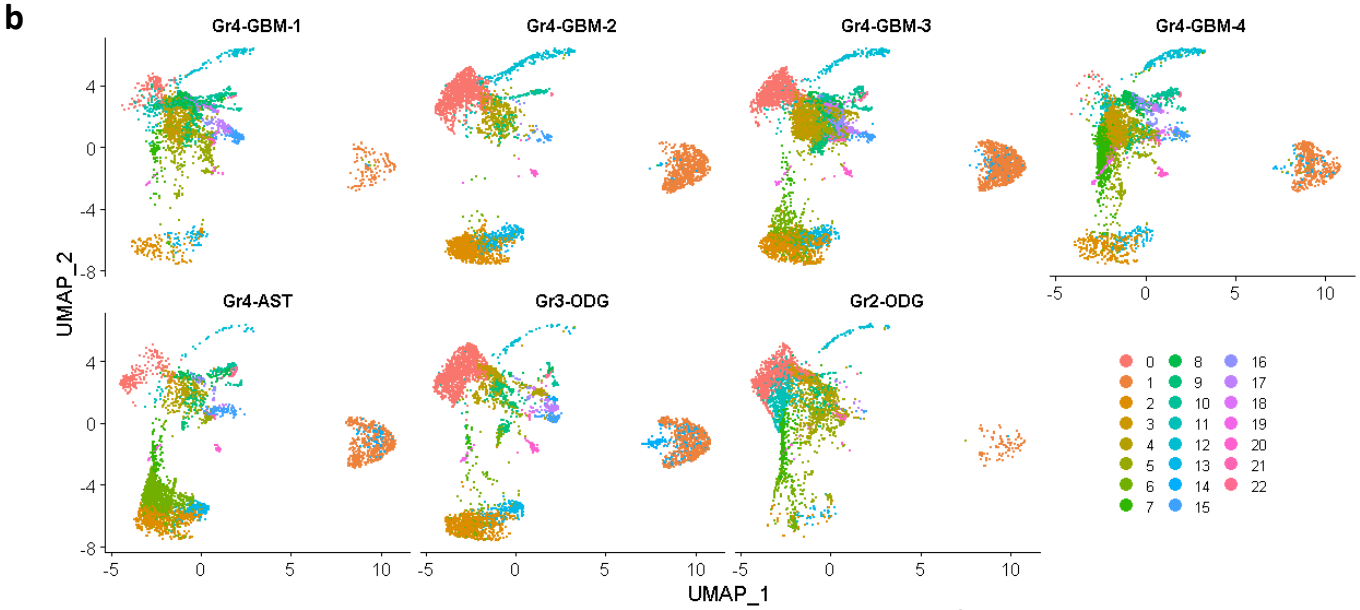

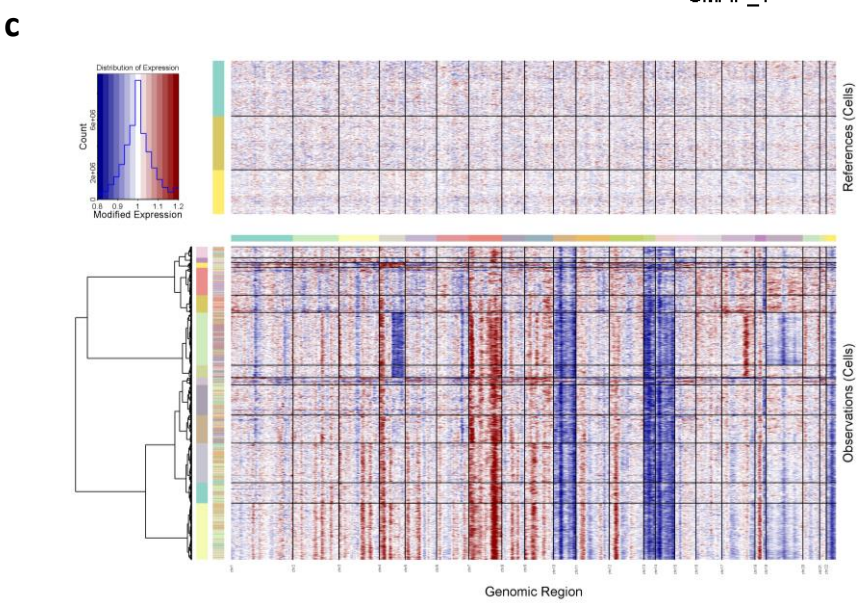

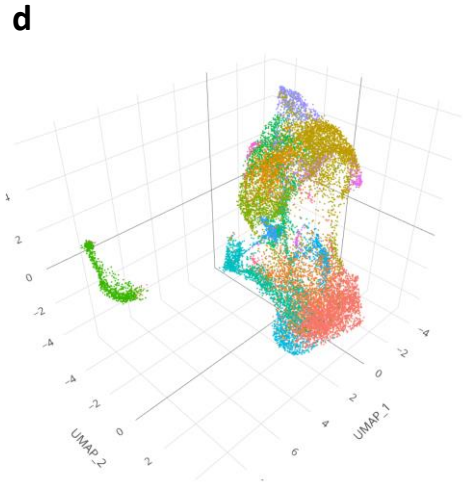

Supplementary Figure 2. Related to Fig. 2

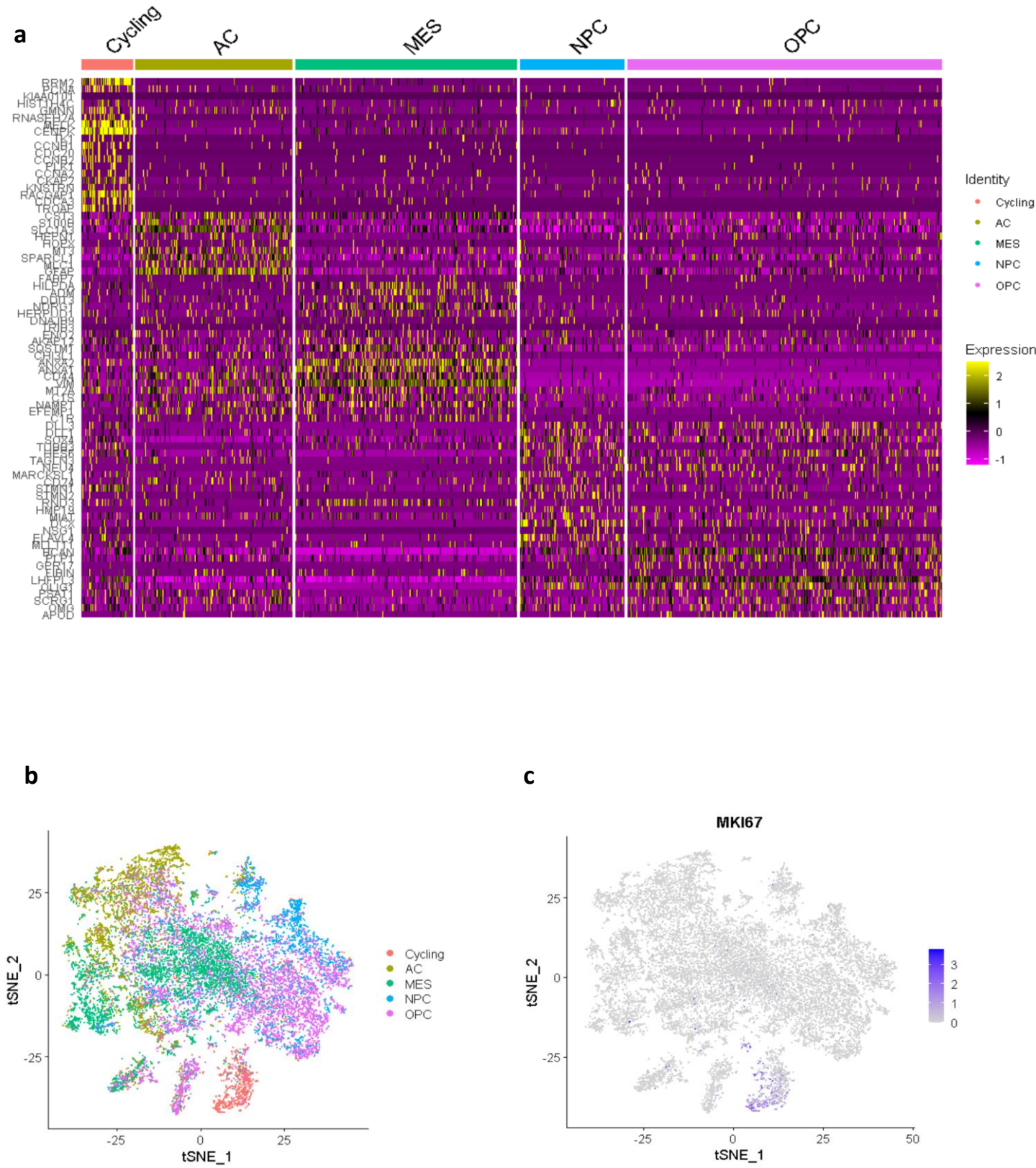

Supplementary Figure 3. Related to Fig. 3

a

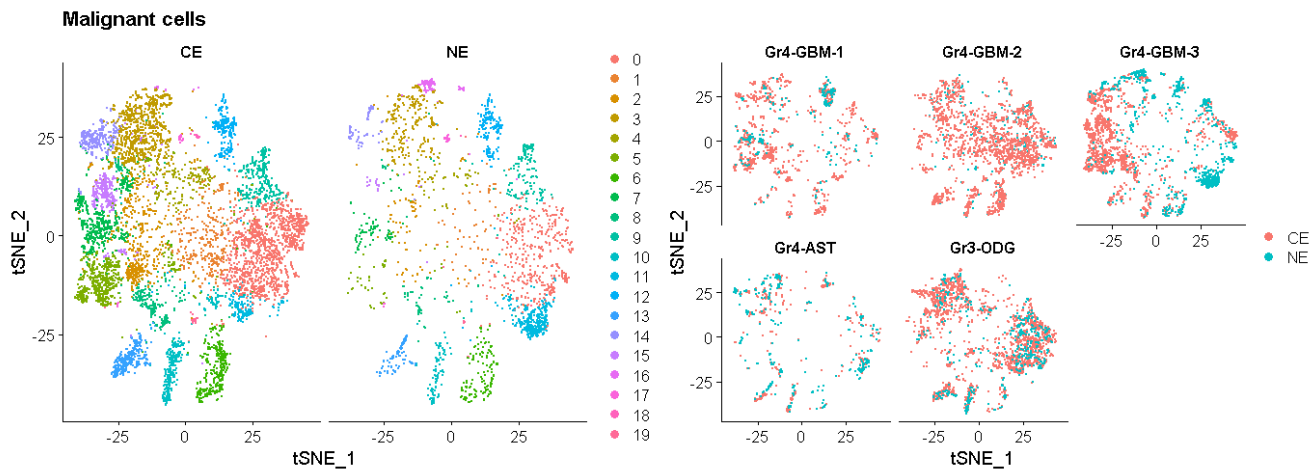

b

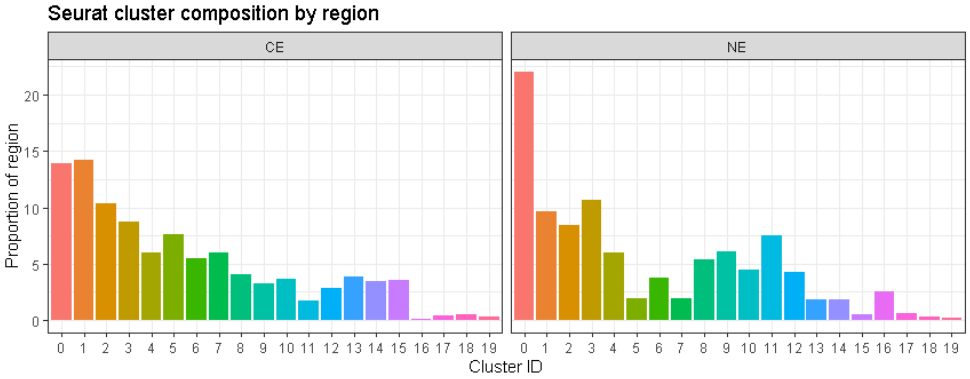

c

IHC Biopsy Patients	
No. patients	17
Age (range)	52 (29-70)
Gender	13 M (76%) 4 F (34%)
WHO Grade	
III	8 (47%)
IV	9 (53%)

d

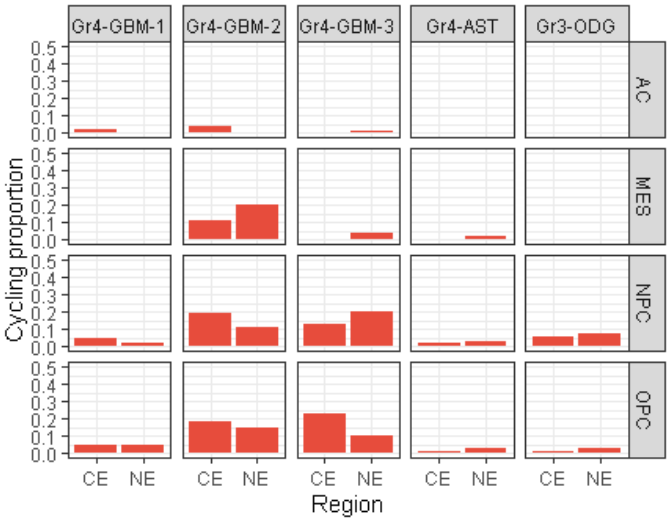

e

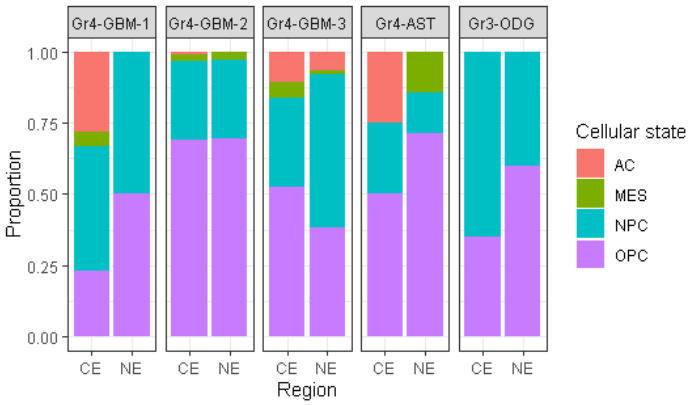

Supplementary Figure 4. Related to Fig. 4

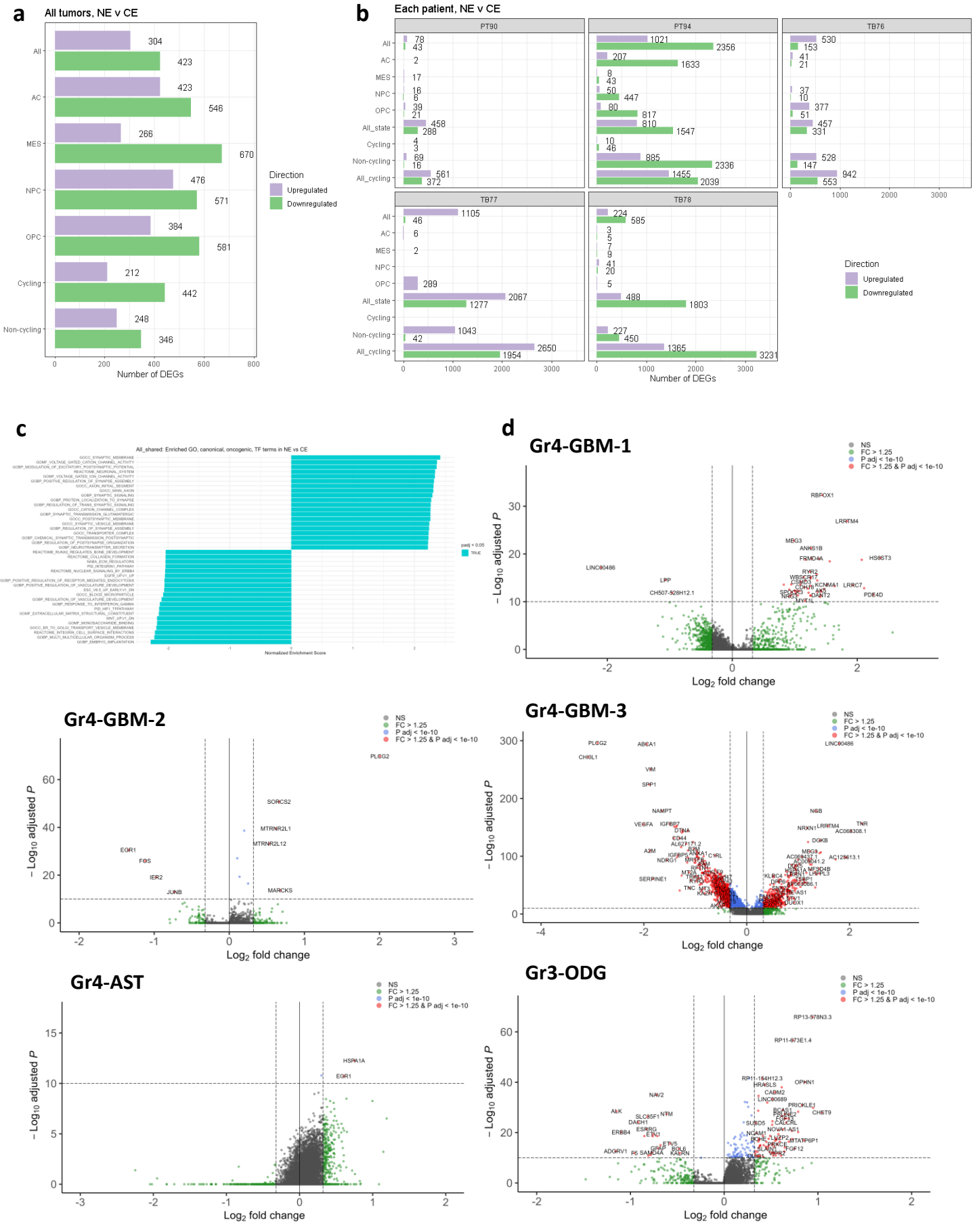

e

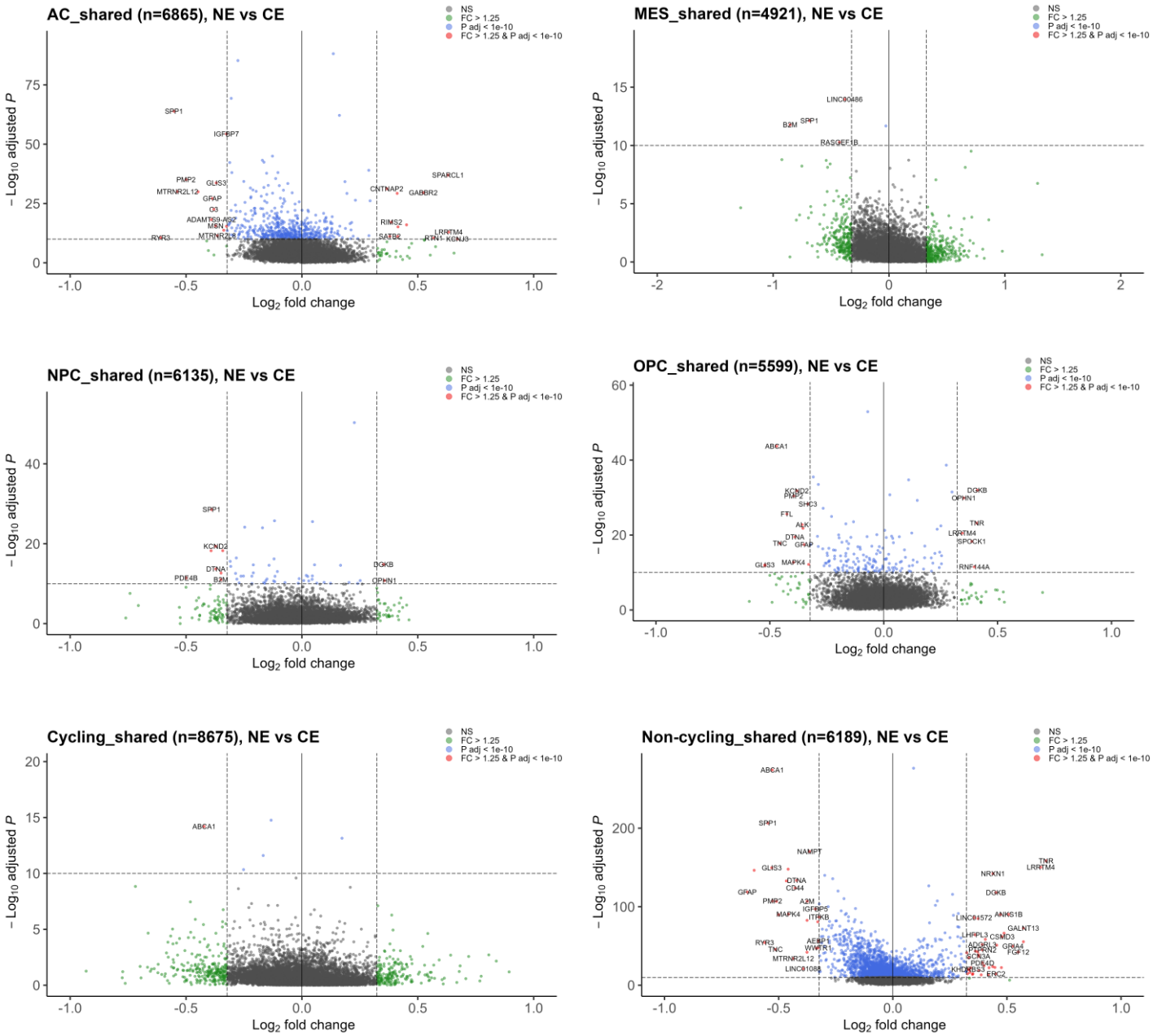
AC_shared (n=6865), NE vs CE
MES_shared (n=4921), NE vs CE
NPC_shared (n=6135), NE vs CE
OPC_shared (n=5599), NE vs CE
Cycling_shared (n=8675), NE vs CE
Non-cycling_shared (n=6189), NE vs CE
NS
FC > 1.25
P adj < 1e-10
FC > 1.25 & P adj < 1e-10
− Log10 adjusted P
Log2 fold change

f

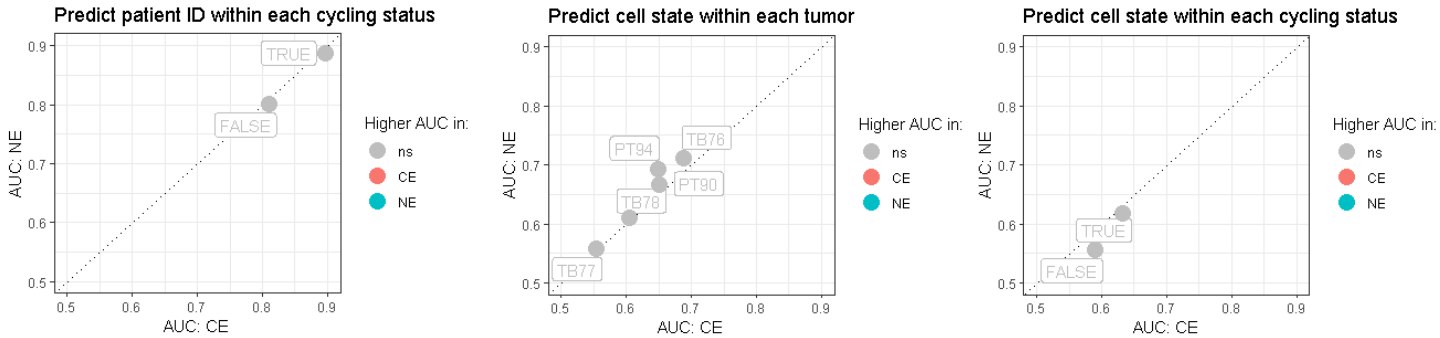
Predict patient ID within each cycling status
Predict cell state within each tumor
Predict cell state within each cycling status
TRUE
FALSE
PT94
TB76
PT90
TB78
TB77
Higher AUC in:
ns
CE
NE
AUC: NE
AUC: CE

Supplementary Figure 5. Related to Fig. 5

a

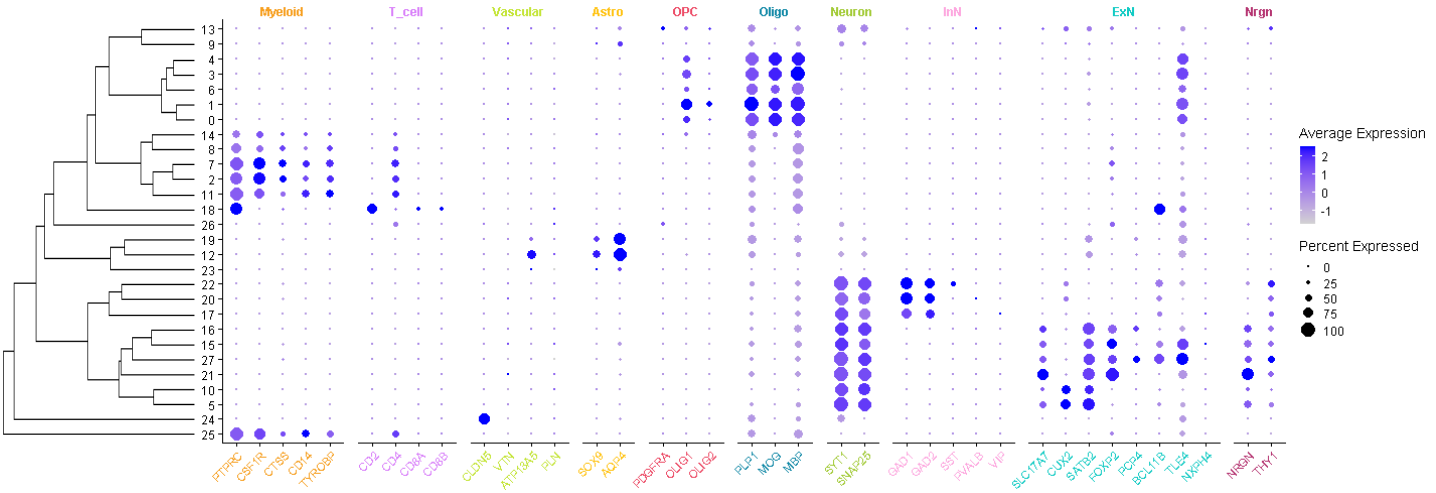

b

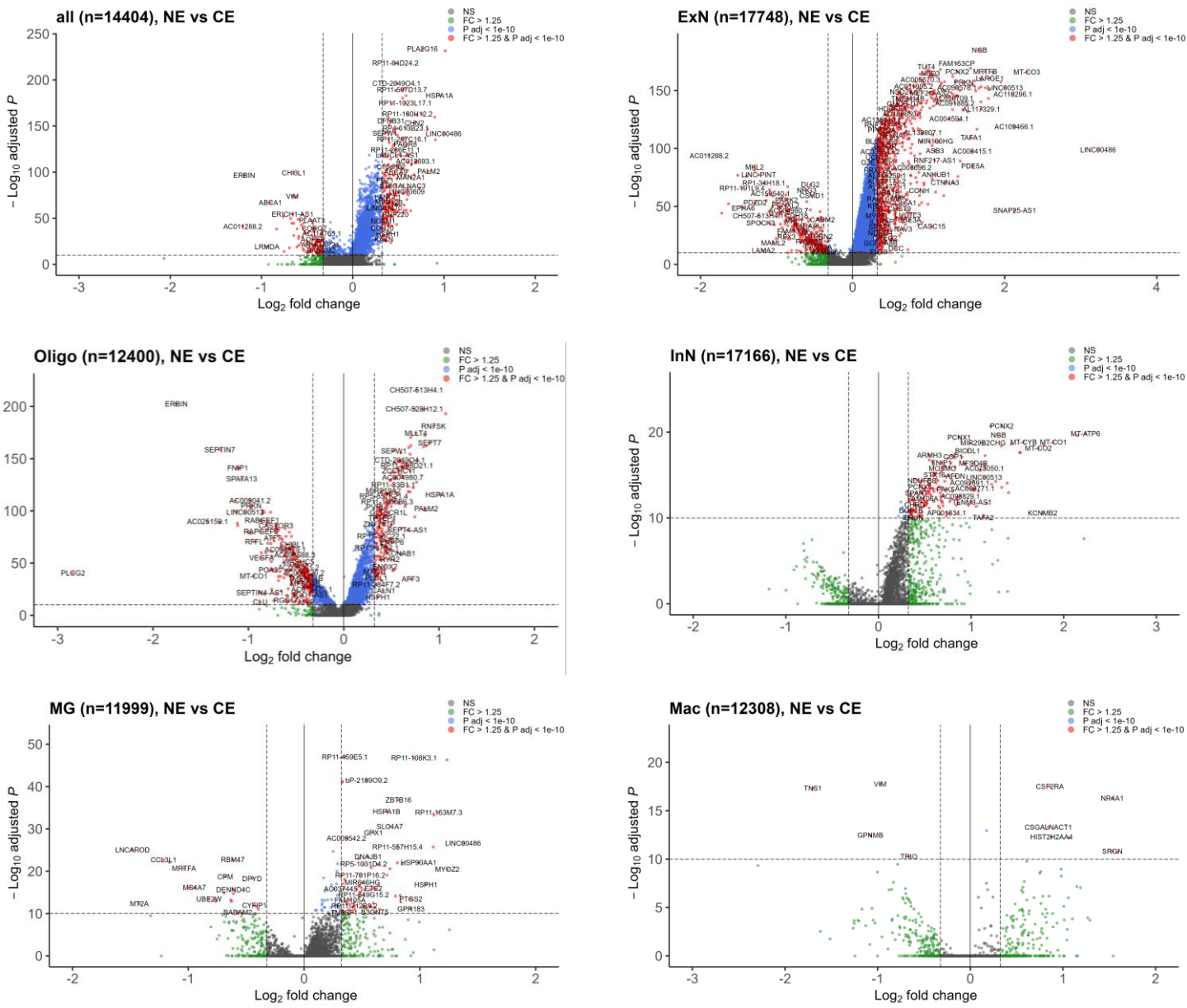

c

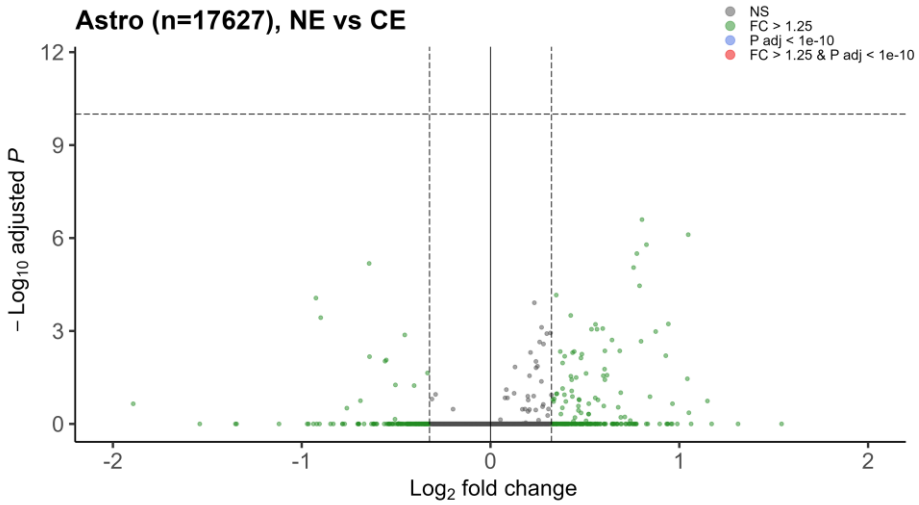
Astro (n=17627), NE vs CE
NS
FC > 1.25
P adj < 1e-10
FC > 1.25 & P adj < 1e-10
– Log10 adjusted P
Log2 fold change

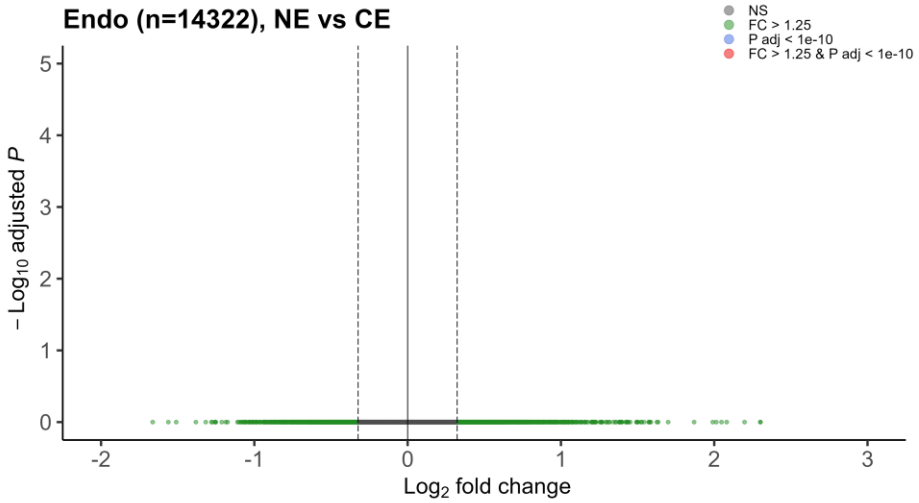
Endo (n=14322), NE vs CE
NS
FC > 1.25
P adj < 1e-10
FC > 1.25 & P adj < 1e-10
– Log10 adjusted P
Log2 fold change

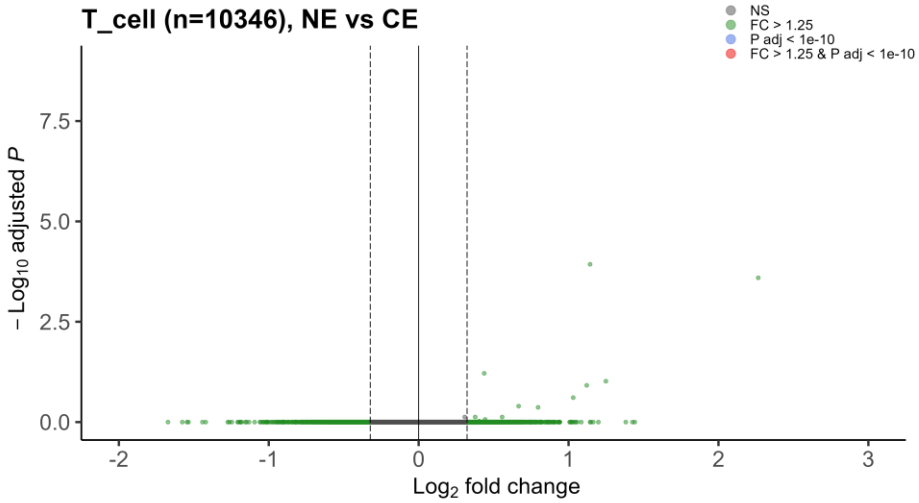
T_cell (n=10346), NE vs CE
NS
FC > 1.25
P adj < 1e-10
FC > 1.25 & P adj < 1e-10
– Log10 adjusted P
Log2 fold change

Supplementary Figure 6. Related to Fig. 6

a

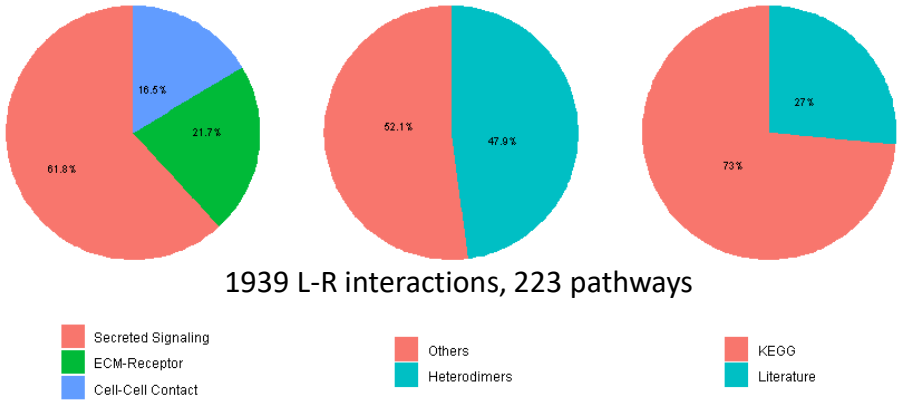

b

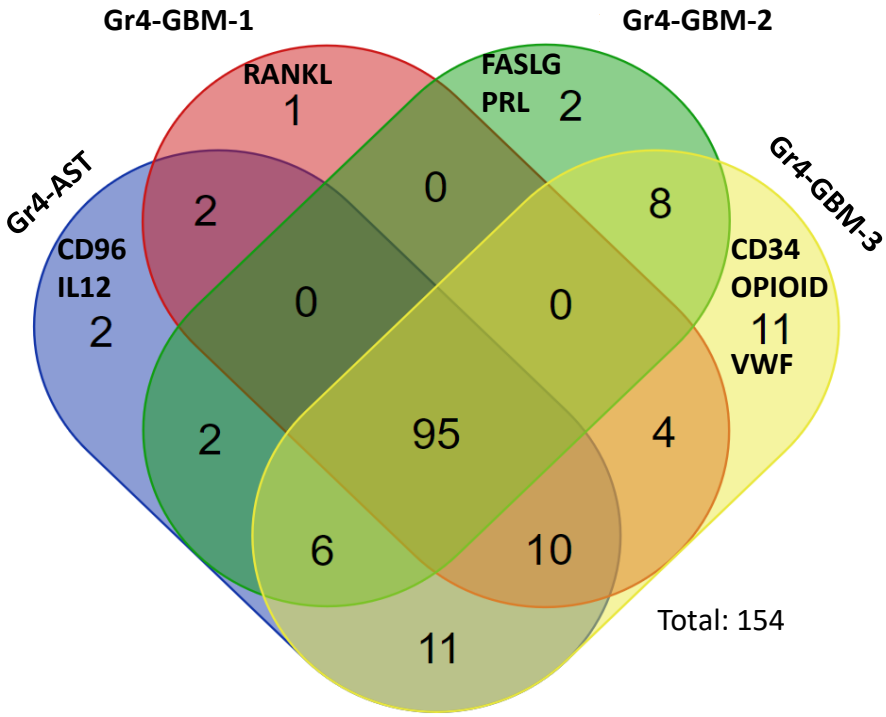

c

	Gr4-GBM-1	Gr4-GBM-2	Gr4-GBM-3	Gr4-AST
total identified	112	113	145	128
altered information flow #	60	58	69	52
altered information flow %	53.6	51.3	47.6	40.6
CE-enriched #	43	28	37	18
CE-enriched %	38.4	24.8	25.5	14.1
NE-enriched #	17	30	32	34
NE-enriched %	15.2	26.5	22.1	26.6

Supplementary Figure 7. Related to Fig. 7

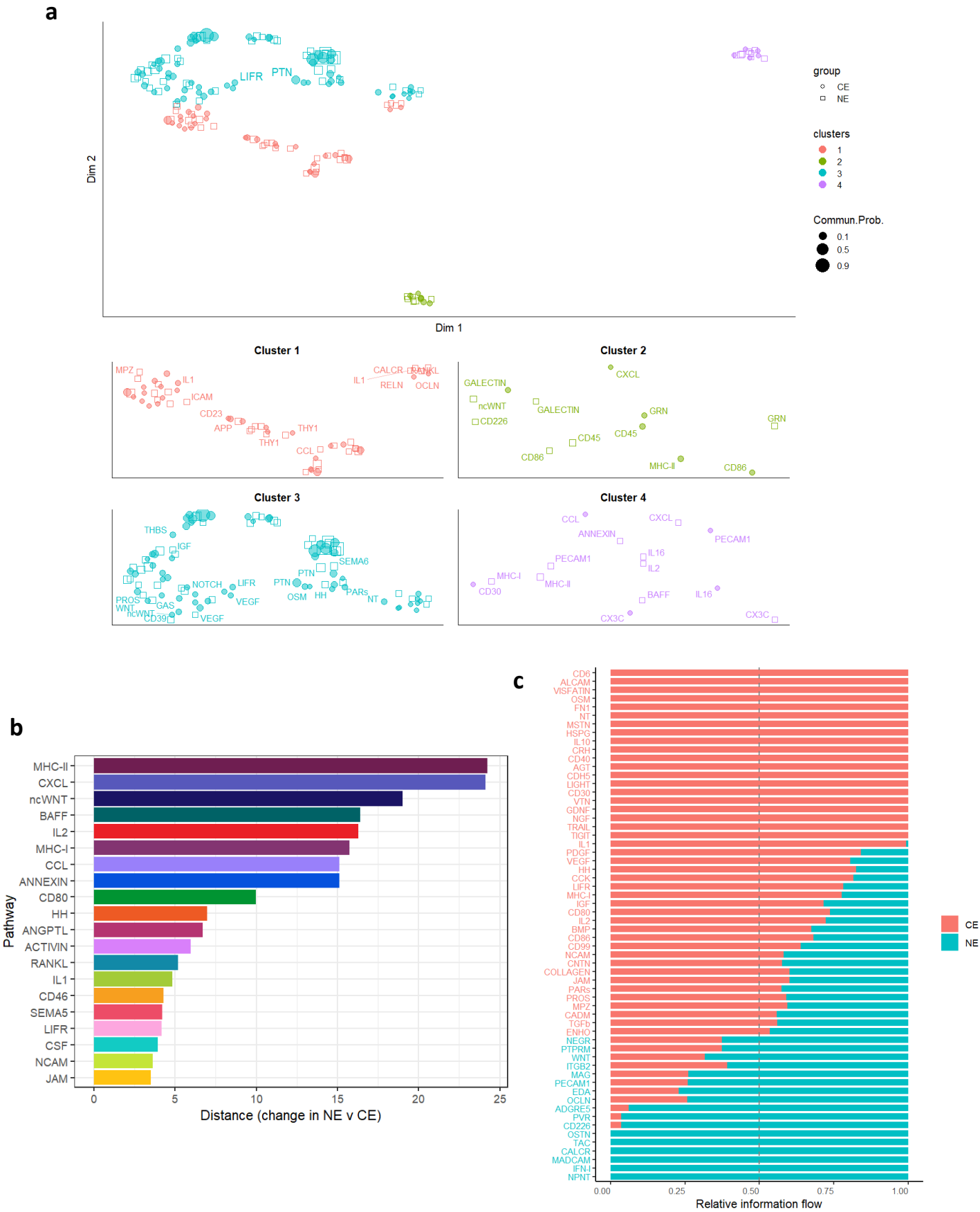

Supplementary Figure 7. Related to Fig. 7

d

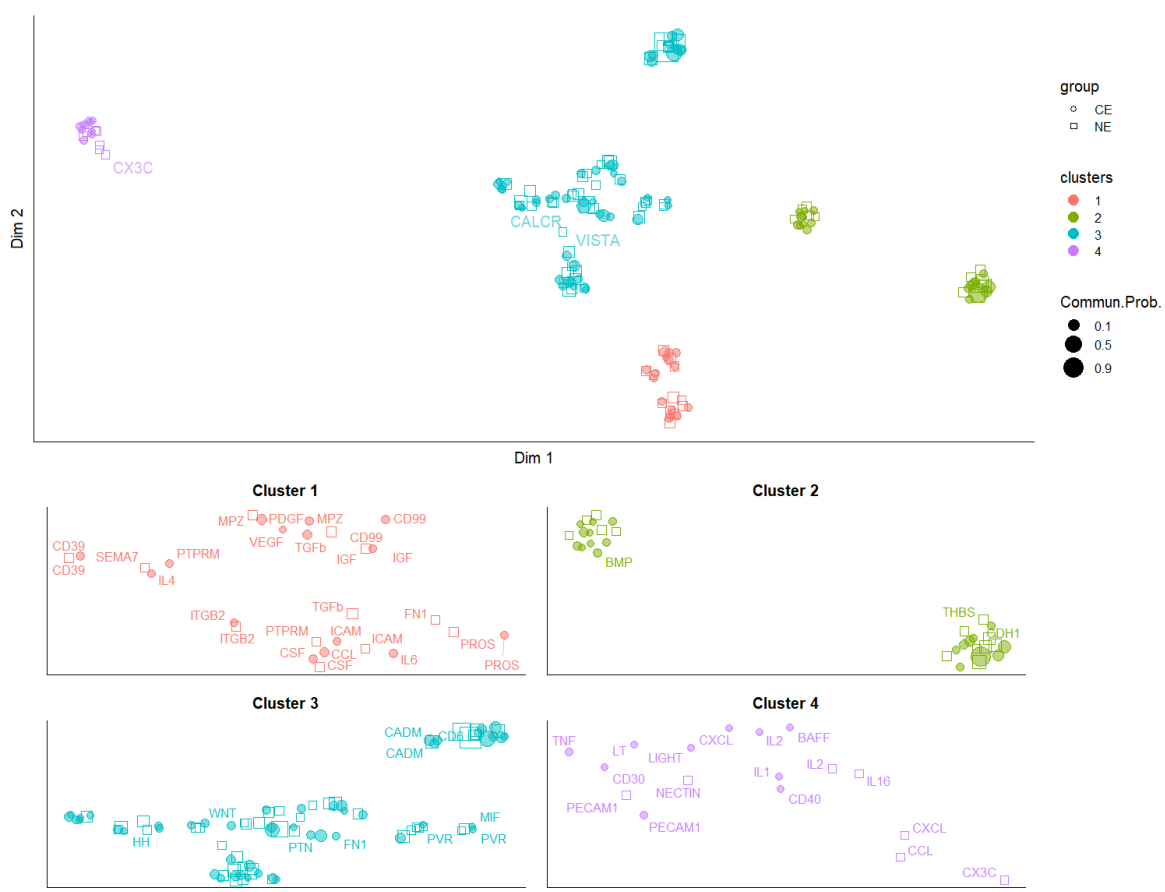

e

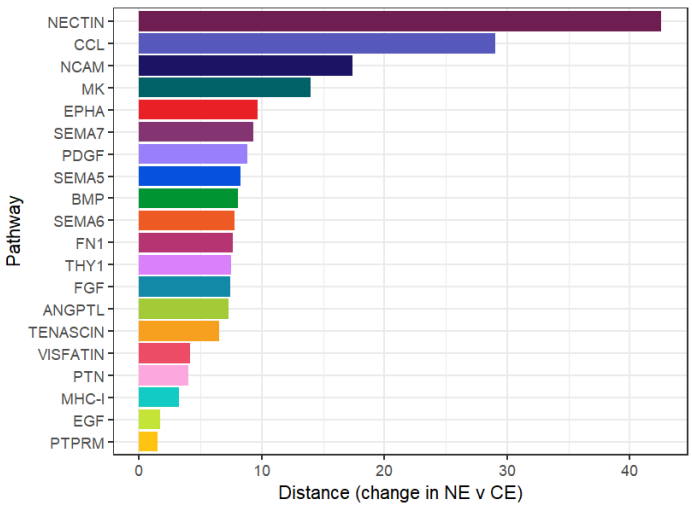

f

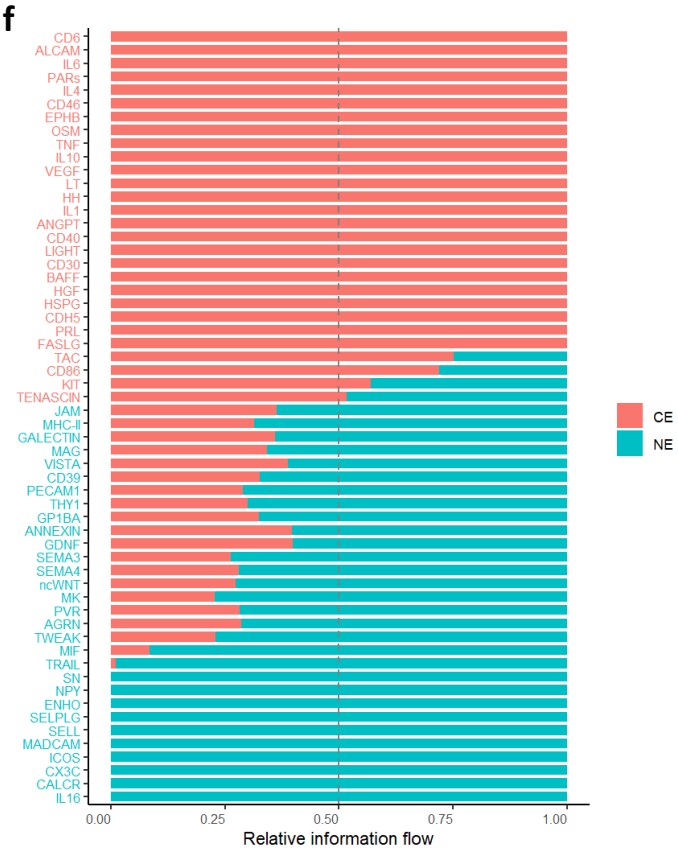

Supplementary Figure 7. Related to Fig. 7

g

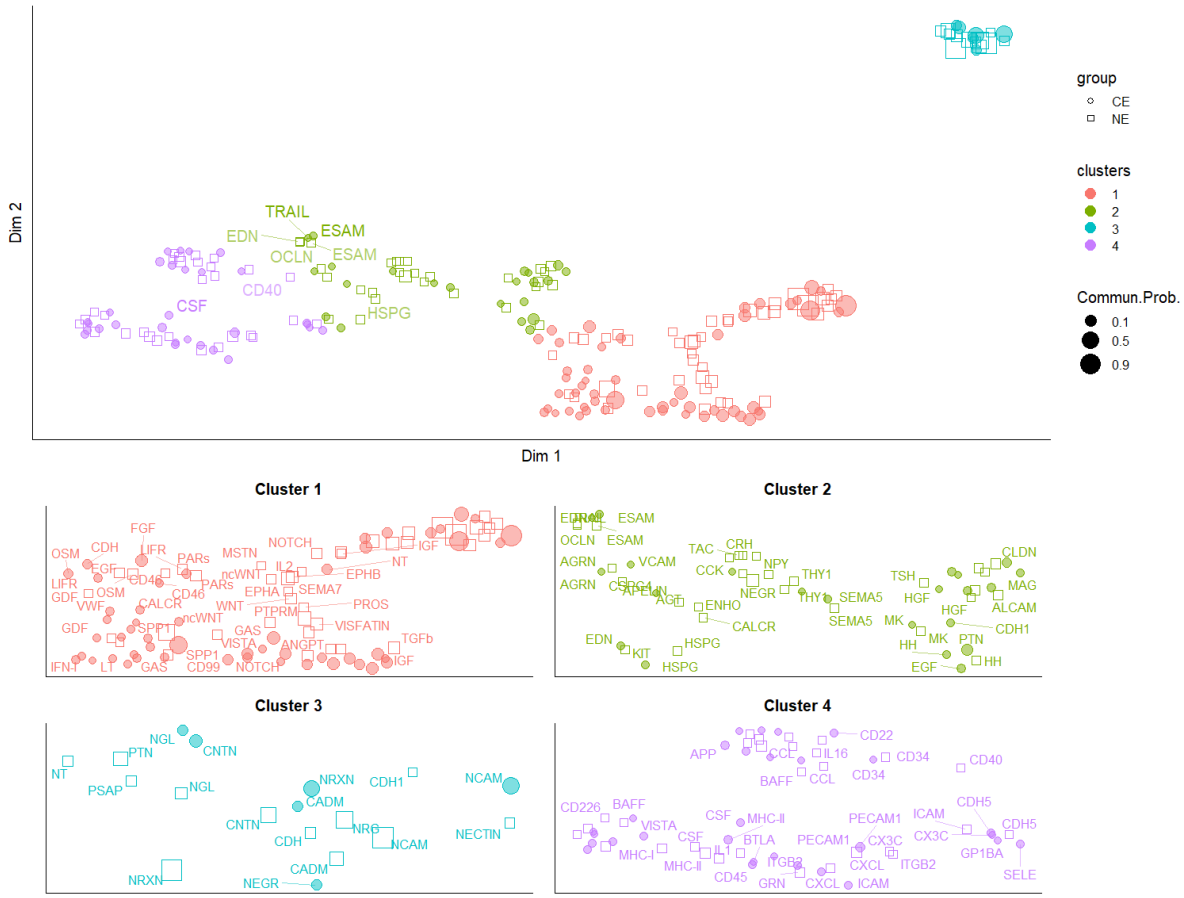

h

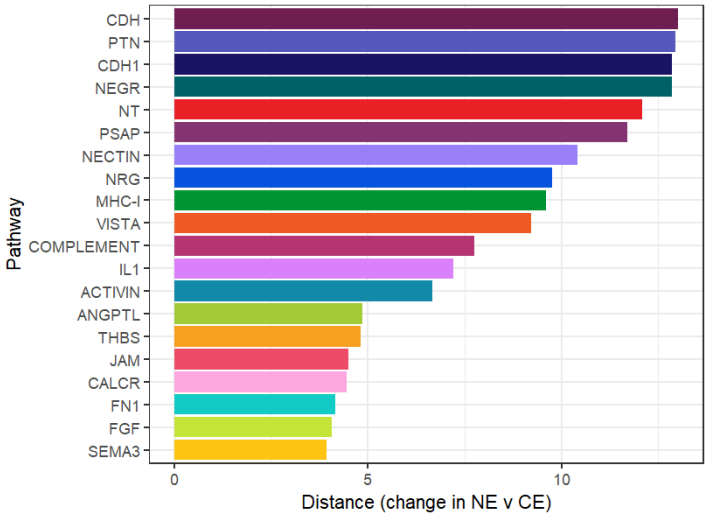

i

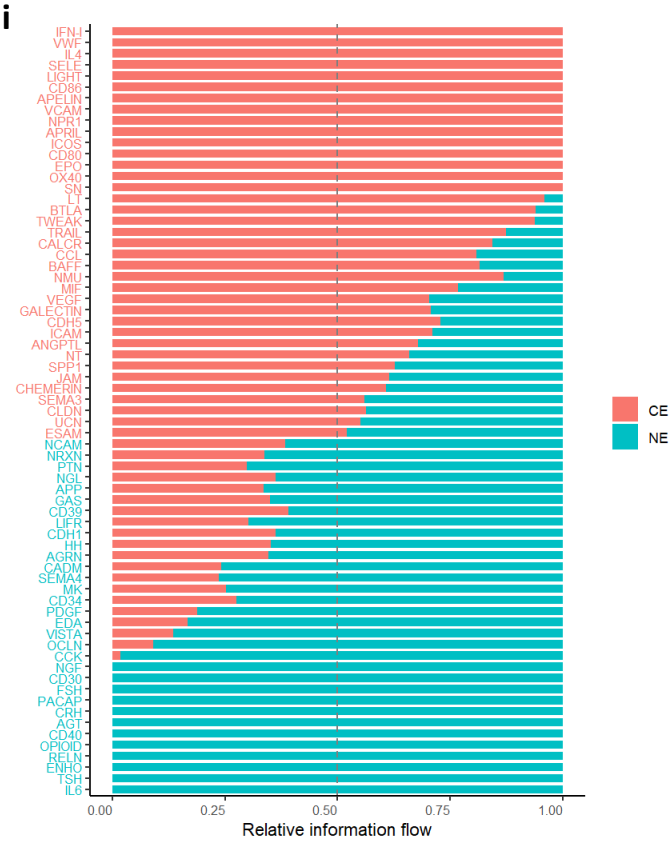

Supplementary Figure 7. Related to Fig. 7

j

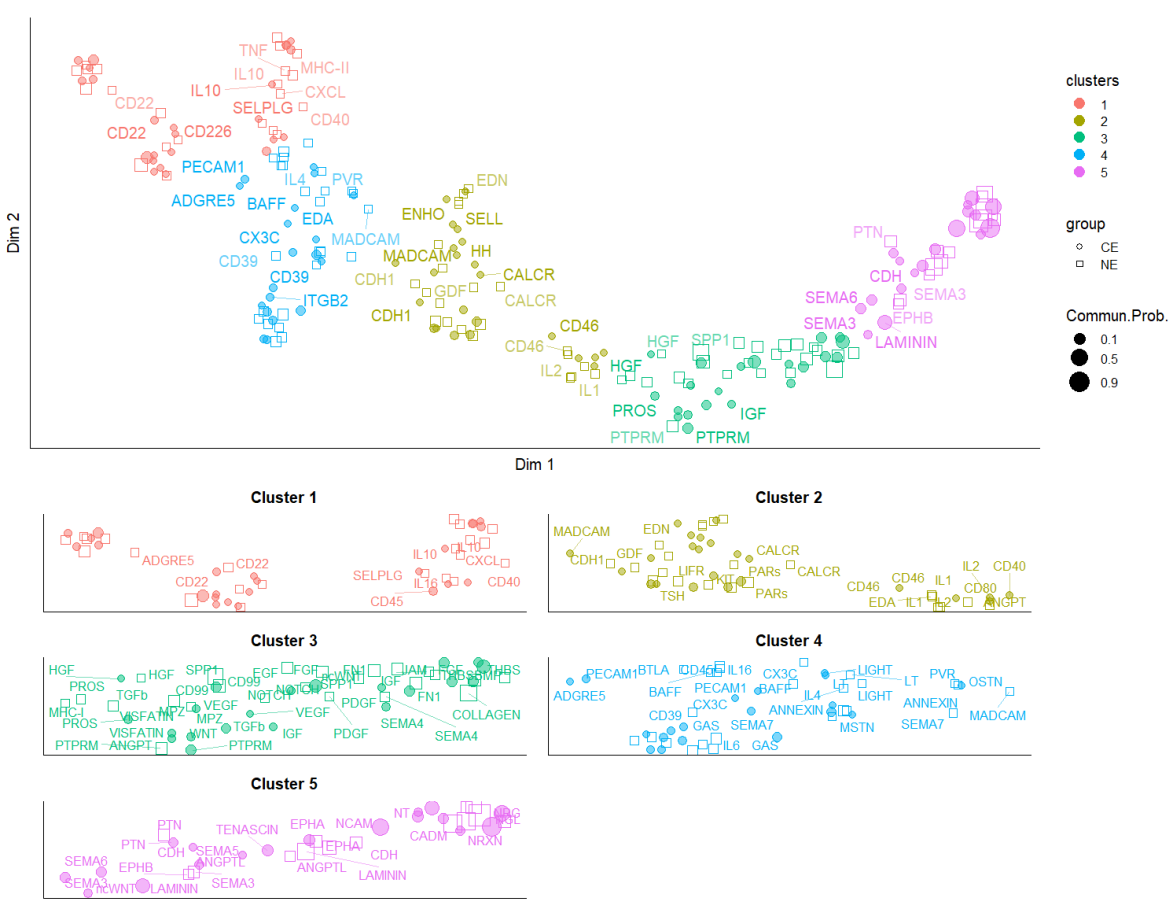

k

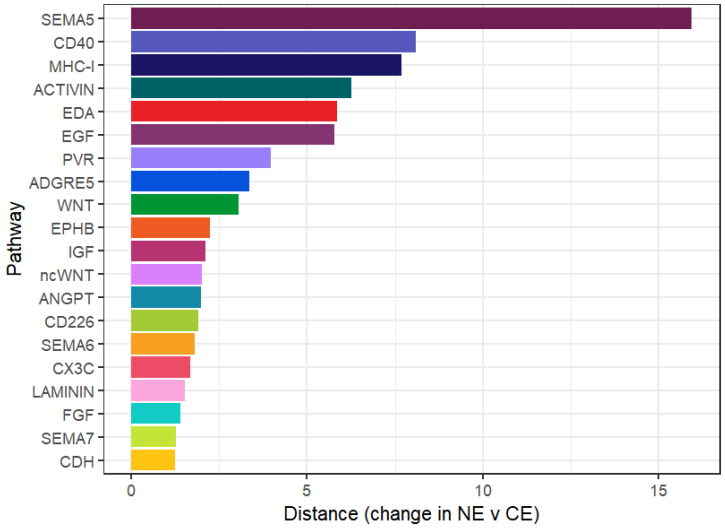
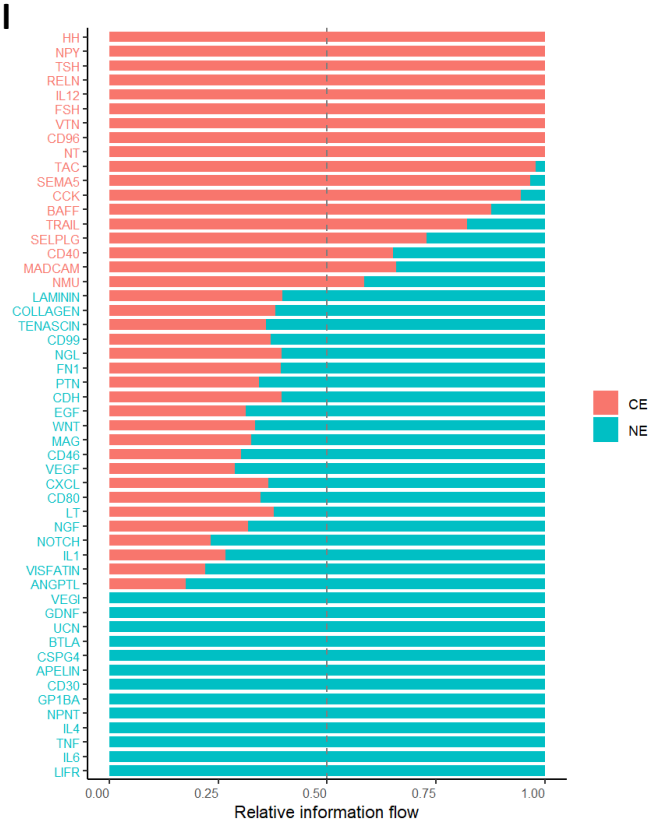
l